Monthly Notices of the ROYAL ASTRONOMICAL SOCIETY

MNRAS **526,** 2378–2393 (2023) https://doi.org/10.1093/mnras/stad2896
Advance Access publication 2023 September 22

Chemical abundances of the young inner-disc open cluster NGC 6705 observed by APOGEE: sodium-rich and not α-enhanced

V. Loaiza-Tacuri [1]★ K. Cunha,[1,2,3] D. Souto,[4] V. V. Smith,[3,5] R. Guerço [1] C. Chiappini,[6] J. V. Sales-Silva,[1] D. Horta [7] C. Allende Prieto,[8] R. Beaton,[9] D. Bizyaev [10,11] S. Daflon,[1] P. Frinchaboy,[12] S. Hasselquist,[13] C. R. Hayes [14] J. A. Holtzman,[15] H. Jönsson,[16] S. R. Majewski,[17] S. Mészáros,[18,19] D. L. Nidever,[20] M. Pinsonneault [21] and G. Zasowski[22]

Affiliations are listed at the end of the paper

Accepted 2023 September 19. Received 2023 September 12; in original form 2023 June 20

ABSTRACT

Previous results in the literature have found the young inner-disc open cluster NGC 6705 to be mildly α-enhanced. We examined this possibility via an independent chemical abundance analysis for 11 red-giant members of NGC 6705. The analysis is based on near-infrared APOGEE spectra and relies on LTE calculations using spherical model atmospheres and radiative transfer. We find a mean cluster metallicity of [Fe/H] $= +0.13 \pm 0.04$, indicating that NGC 6705 is metal-rich, as may be expected for a young inner-disc cluster. The mean α-element abundance relative to iron is $\langle[\alpha/\mathrm{Fe}]\rangle = -0.03 \pm 0.05$, which is not at odds with expectations from general Galactic abundance trends. NGC 6705 also provides important probes for studying stellar mixing, given its turn-off mass of $M \sim 3.3\,\mathrm{M}_{\odot}$. Its red giants have low ^{12}C abundances ([^{12}C/Fe] $= -0.16$) and enhanced ^{14}N abundances ([^{14}N/Fe] $= +0.51$), which are key signatures of the first dredge-up on the red giant branch. An additional signature of dredge-up was found in the Na abundances, which are enhanced by [Na/Fe] $= +0.29$, with a very small non-LTE correction. The ^{16}O and Al abundances are found to be near-solar. All of the derived mixing-sensitive abundances are in agreement with stellar models of approximately $3.3\,\mathrm{M}_{\odot}$ evolving along the red giant branch and onto the red clump. As found in young open clusters with similar metallicities, NGC 6705 exhibits a mild excess in the s-process element cerium with [Ce/Fe] $= +0.13 \pm 0.07$.

Key words: stars: abundances – infrared: stars – Galaxy: inner disc – stars: giants – stars: open cluster.

1 INTRODUCTION

Open clusters are excellent probes of chemical evolution in the Milky Way disc, as their range in metallicity overlaps that of the disc field stars, while their locations extend from the inner disc to the outskirts of the Galaxy, and they have formed over an extended period of Galactic history. NGC 6705 (Messier 11, M11) is relatively star-rich, compact, and located in the inner disc at a Galactocentric distance of 6.5 kpc (Cantat-Gaudin et al. 2020). This open cluster is young, with a well-defined age from isochrone fitting of 316 ± 50 Myr (Cantat-Gaudin et al. 2014; Dias et al. 2021) and, given its youth, has probably not migrated very far from its birthplace, with an estimated birth radius between 6.8–7.5 kpc (Casamiquela et al. 2018).

NGC 6705 has been reported to be a metal-rich cluster, with [Fe/H] $\sim +0.1$–0.17 (e.g.; Gonzalez & Wallerstein 2000; Heiter et al. 2014; Magrini et al. 2017; Casamiquela et al. 2018), although recent works have also found it to have mean metallicities closer to solar (Casamiquela et al. 2021; Magrini et al. 2021; Randich et al. 2022). Another aspect of this open cluster is that previous studies in the literature (Tautvaišienė et al. 2015; Casamiquela et al. 2018) have found its stellar members to be moderately enhanced in α-elements relative to iron ([α/Fe] $\sim +0.1$ to $+0.2$), although it has an age of only a few hundred million years. Magrini et al. (2014) also found NGC 6705 to be mildly enhanced in α-elements: $<[\alpha/\mathrm{Fe}]> = +0.08$, while the more recent study of Magrini et al. (2017) found that only [Mg/Fe], and not the other α-elements, was enhanced (by $+0.1$ dex) in NGC 6705.

Youth and α-enhancement together are not expected from simple chemical evolution modelling, as α-elements, such as O, Mg, Si, and Ca are produced at early times, mainly in Type II Supernovae (formed by massive stars on short timescales); enrichment in the [α/Fe] ratio generally indicates that a star formed from gas enriched by SN II before SN Ia had the time to contribute iron to the natal gas. Within the Galactic disc, there are two sequences defined by the α-element abundances: the high- and the low-α sequences (e.g. Fuhrmann 1998; Reddy, Lambert & Allende Prieto 2006; Anders et al. 2014; Nidever et al. 2014; Hayes et al. 2018; Queiroz et al. 2020); the high-α sequence is older and corresponds to the thick disc (rich in α-elements relative to its Fe content), while the thin disc population consists of stars with lower values of [α/Fe].

There are, however, interesting results in the literature pointing to a population of young field stars with a high abundance ratio of α-element-to-iron, which are unusual given their ages reported in the literature. Chiappini et al. (2015) discovered such young [α/Fe]-enhanced stars in a sample of field stars observed by the SDSS APOGEE Survey (Majewski et al. 2017) having CoRoT asteroseismology (Baglin et al. 2006). CoRoT provided precise age

★ E-mail: vtacuri@on.br

estimation for field stars, resulting in the identification of a large number of young stars in the inner region of the Galactic disc that are rich in α-elements ([α/Fe] $\sim$ 0.1–0.3) and with a low abundance of iron-peak elements. Meanwhile, Martig et al. (2015) analysed a sample of 1639 red giants with astereoseismic ages from the APOGEE sample and observed by the Kepler mission (referred to as the APOKASC sample) to investigate the relationship between age and chemical abundances. As a result of their analysis, they identified fourteen stars enriched in α-elements ([α/Fe] $>$ 0.13) that were younger than 6 Gyr, and five stars with [α/Fe] $\geq$ 0.20 are younger than 4 Gyr. Possible scenarios to explain this young, α-enhanced population of stars include accretion of material from a binary companion or binary mergers (e.g. Izzard et al. 2018; Silva Aguirre et al. 2018; Hekker & Johnson 2019; Jofré et al. 2023), resulting in stars that would appear to be young, while actually being old. In addition, Miglio et al. (2021) found that stars with [α/Fe] $>$ 0.1 from the Kepler field that appeared young were overmassive; this result supports the scenario that most of these stars have undergone an interaction with a companion.

Given its youth, coupled to the mild α-enhancements found for NGC 6705 in the literature (Tautvaišienė et al. 2015; Casamiquela et al. 2018), along with the different signatures (α-enhanced versus non α-enhanced) obtained, for example, for Mg in comparison with other α-elements (Magrini et al. 2017), and the relevance of finding a young α-rich open cluster in the context of the young α-enhanced field stars in the Galaxy (as discussed in Casamiquela et al. 2018), it becomes important to revisit the α-abundances in NGC 6705 from a completely independent analysis, also keeping in mind that the results in the literature for NGC 6705 mentioned above are all from optical studies. All, except for Casamiquela et al. (2018), being based on the Gaia-ESO survey (GES; Gilmore et al. 2012, 2022; Randich et al. 2022).

In addition, due to its relative youth and stellar richness in comparison to other open clusters, NGC 6705 contains a populous sample of red giants in which to probe stellar mixing in the interesting mass range between $M \sim 3.0$–$3.5\,M_{\odot}$. Such intermediate-mass red giants can exhibit measurable chemical abundance changes due to deep mixing beyond the usual variations in ^{12}C, ^{13}C, and ^{14}N observed in lower-mass red giants, to include possible changes in the ^{16}O, or Na, or Al abundances. The red giants in NGC 6705 can provide an important observational test of stellar models. Smiljanic et al. (2016) studied Na and Al in low- and intermediate-mass clump giants, in particular in six open clusters from the Gaia ESO survey, and found both Na and Al to be enriched in NGC 6705. While their Na results for this cluster were in agreement with predictions from stellar evolution models, their Al abundances were above model predictions, as aluminium is not expected to be affected by mixing in the mass range of NGC 6705 giants (Lagarde et al. 2012).

In this study, we select a sample of red giant stars that are members of NGC 6705 in order to determine their stellar parameters and present a detailed analysis of the chemical abundances of their α-elements (O, Mg, Si, Ca, and Ti), along with iron and the Fe-peak elements (V, Cr, Mn, Co, and Ni), elements sensitive to red giant mixing (^{12}C, ^{14}N, Na, and Al), as well as the s-process element cerium. This spectroscopic analysis is based on APOGEE spectra, which are in the near-infrared, but uses an independent analysis and methodology when compared with the APOGEE abundance pipeline ASPCAP (García Pérez et al. 2016), particularly in the derivation of the stellar parameters effective temperature and surface gravity, and given the well-known systematic offsets in surface gravity values for the ASPCAP results, which are post-calibrated (Jönsson et al. 2020). This paper is organized as follows: in Section 2, we present the sample and the observations, while Section 3 describes the methodology to determine the stellar parameters, and Section 4 presents the individual abundance analysis of seventeen elements. In Section 5, we compared our results with literature results. Section 6 contains a discussion of the results, and Section 7 the conclusions.

2 OBSERVATION AND SAMPLE

2.1 APOGEE spectra

The Apache Point Observatory Galactic Evolution Experiment (APOGEE; Majewski et al. 2017) was one of the three surveys carried out as part of the Sloan Digital Sky Survey-IV (SDSS-IV; Blanton et al. 2017). APOGEE targeted the open cluster NGC 6705 as part of its OCCAM (Open Cluster Chemical Abundances and Mapping) campaign, which aimed to study the structure and chemical evolution of the Milky Way (Frinchaboy et al. 2013; Donor et al. 2018; Myers et al. 2022). The APOGEE spectra analysed in this study were obtained using a 300-fiber cryogenic spectrograph on the 2.5-m telescope at the Apache Point Observatory (New Mexico, USA; Gunn et al. 2006), and these have a resolution $R = \lambda/\Delta\lambda \sim 22\,500$ and spectral coverage from 1.51 to 1.69 µm (Wilson et al. 2010, 2019). Reduction of the APOGEE spectra, as well as the determination of the stellar radial velocities, were carried out by an automated data processing pipeline (Nidever et al. 2015), and the reduced spectra analysed here come from the publicly available 17th APOGEE data release (DR17; Abdurro'uf et al. 2022). The open cluster NGC 6705 was observed in APOGEE field 027–04, identified by location ID 4470 (Zasowski et al. 2013, 2017; Beaton et al. 2021). APOGEE targeted a total of 343 stars in this field, which were investigated here for cluster membership in the section below.

2.2 NGC 6705 membership

The open cluster NGC 6705 is located at Galactic coordinates $l = 27.304°$ and $b = -2.773°$ at an estimated distance of $\sim$1900–2200 pc (e.g. Cantat-Gaudin & Anders 2020; Dias et al. 2021; Hunt & Reffert 2023). The mean radial velocity of its cluster members, according to radial velocities from *Gaia* DR2, was estimated in Dias et al. (2021) to be $35.68 \pm 0.24\,\mathrm{km\,s^{-1}}$ and considering 357 stars Tarricq et al. (2021) found a mean radial velocity of $34.49 \pm 0.27\,\mathrm{km\,s^{-1}}$.

2.2.1 *Membership according to HDBSCAN*

We used the PYTHON code HDBSCAN (Hierarchical Density-Based Spatial Clustering of Applications with Noise; Campello, Moulavi & Sander 2013) clustering algorithm to independently assess which stars from the observed APOGEE field 027–04 would be identified as members of the NGC 6705 open cluster. HDBSCAN is an unsupervised machine learning method, which does not require learning from labelled data to make predictions. More specifically, HDBSCAN is a density-based clustering algorithm that groups data points together based on their proximity and density.

HDBSCAN uses a number of input parameters that can be adjusted to control its clustering estimations. The main input parameters are: *min_cluster_size*, *min_samples*, *cluster_selection_epsilon*, and *alpha*. The parameter *min_cluster_size* sets the minimum number of points needed to define a distinct cluster; thus, any potential cluster that might contain fewer points would be labelled as noise (outliers). The *min_samples* parameter defines the minimum number of neighbouring points surrounding a given point for it to be considered as a core

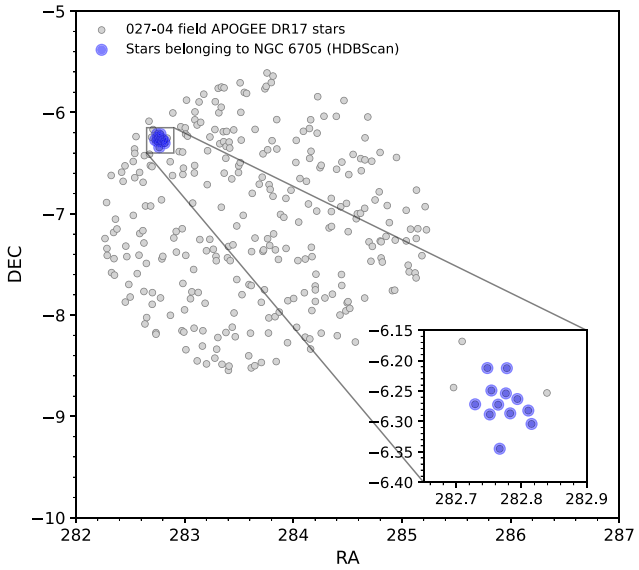

Figure 1. Declination (DEC) versus right ascension (RA) of stars from 027–04 field – APOGEE DR17. The stars highlighted in blue are the stars pointed out as members of the NGC 6705 cluster using the HDBSCAN code. The highlighted panel is a region zoom containing these stars.

point, while a minimum distance below which HDBSCAN will not further split a cluster is set by the parameter *cluster_selection_epsilon*. The parameter *alpha* controls the balance between condensed tree density and hierarchy depth. Higher values of *alpha* result in clusters that are more tightly bound within the hierarchy, while lower values allow clusters to be more easily split. For the APOGEE field 027–04, we used the following parameter values: *min_cluster_size* = *4*, *min_samples* = *3*, *cluster_selection_epsilon* = *0.0*, and *alpha* = *1.0*.

To search for cluster members within the observed stars in the APOGEE plate, we used three parameters: proper motions (pm RA and pm DEC) from *Gaia* DR3 (*Gaia* DR3; Gaia Collaboration 2021), distances from Bailer-Jones et al. (2021), and radial velocities from APOGEE DR17. As mentioned above, the APOGEE 027–04 field has 343 stars, however, not all of them have all three parameters available. Fig. 1 shows the RA-DEC space of the 307 stars analysed with the HDBSCAN code. From this group, twelve stars have been selected as cluster members according to our parameters, and these are shown as blue circles in Fig. 1. The results from HDBSCAN indicated that eleven of the stars had 100 per cent probability of being cluster members, while the star 2MASS J18510399-0620414 had a slightly lower probability (93 per cent) of belonging to the cluster.

2.2.2 *Other membership from the literature*

We also investigated which stars observed by APOGEE would be members of NGC 6705, according to other studies in the literature. Thirty one stars have been labelled as possible members of NGC 6705 in the most recent OCCAM study by (Myers et al. 2022) (their Table 3), and the upper right-hand panel of Fig. 2 shows the proper motions of these stars from *Gaia* DR3 (Gaia Collaboration 2021). Their APOGEE radial velocities are shown in the left-hand panel of Fig. 2 and it can be seen that these show a large variation in radial velocities, with RV values ranging mostly between −30–90 km s^{-1}. From this sample of 31 stars, Myers et al. (2022) used APOGEE radial velocities and metallicities, along with *Gaia* proper motions, to estimate membership probabilities to select a sample of twelve stars that were considered to be members of NGC 6705. In Fig. 2, the twelve member stars are depicted inside the red circle in the right-hand panel and within the red dashed lines in the left-hand panel.

We also verified which stars observed by APOGEE would be members of NGC 6705 according to the probabilities of membership provided by Cantat-Gaudin & Anders (2020). There are 1183 stars in that catalog with a probability of cluster membership larger or equal to 0.7. The cross-match of their member list with the APOGEE DR17 data base led to the identification of twelve stars in common. In addition, these same 12 stars are considered as members by Dias et al. (2021) and eleven of them are members according to Jackson et al. (2022).

In summary, we independently identified a sample of twelve bona fide stellar members of NGC 6705, and this membership is in agreement with the results from other independent studies in the literature. The NGC 6705 members are presented in Table 1, along with the star's 2MASS J, H, K_s (Two Micron All Sky Survey; Cutri et al. 2003), and V magnitudes taken from Cantat-Gaudin et al. (2014), Tautvaišienė et al. (2015), Casamiquela et al. (2016), and Zacharias et al. (2005), and *Gaia* magnitudes (G, G_{BP}, and G_{RP}) from *Gaia* DR3 (Gaia Collaboration et al. 2021).

Also included are the radial velocities (RV), along with the RV dispersions derived from individual APOGEE visits, and the signal-to-noise of the APOGEE spectra. We note that the star 2MASS J18510092-0614564 is deemed to be a binary given the scatter in the *Gaia* radial velocity measurements (*Gaia* DR3 RV = 37.45 ± 11.37 km s^{-1}) and will not be analysed in this study.

Finally, in the two lower panels of Fig. 2, we show the ($J - K_s$) versus J and ($G_{BP} - G_{RP}$) versus G diagrams using 2MASS and *Gaia* DR3 photometry for the sample of twelve stars. The red line in both panels represents the PARSEC isochrone (Bressan et al. 2012) for the age and metallicity of NGC 6705 (0.316 Gyr and 0.10 dex, respectively). The location of the stars relative to the isochrones in the colour magnitude diagrams presented indicates that the selected members are probably red-clump stars, although they could also be on the red-giant branch.

3 STELLAR PARAMETERS

The determination of the abundances of chemical elements from stellar spectra relies on fundamental stellar atmospheric parameters, such as the effective temperature (T_{eff}), surface gravity (log g), microturbulence velocity (ξ), and metallicity ([Fe/H]). To derive these stellar parameters, we employed a methodology that is similar to the analysis presented in Souto et al. (2016).

Stellar effective temperatures were derived from the 2MASS (Two Micron All Sky Survey; Cutri et al. 2003) magnitudes J, H, and K_s, and the photometric calibrations of González Hernández & Bonifacio (2009) through the equation:

$$\theta_{eff} = b_0 + b_1 X + b_2 X^2 + b_3 X[\mathrm{Fe/H}] + b_4[\mathrm{Fe/H}] + b_5[\mathrm{Fe/H}]^2, \quad (1)$$

where $T_{eff} = 5040/\theta_{eff}$, the values X represent the colours $V - J$, $V - H$, $V - K_s$, and $J - K_s$, and the constants b_0, b_1, b_2, b_3, b_4, and b_5 for each photometric colour can be found in González Hernández & Bonifacio (2009). The adopted metallicity in this step was [Fe/H] = 0.10 dex (taken from Cantat-Gaudin et al. (2014)).

The reddening value adopted in this study was $E(B - V)$ = 0.4 (Cantat-Gaudin et al. 2014) and reddening corrections were computed using the relations in Bilir et al. (2008). Table 2 lists

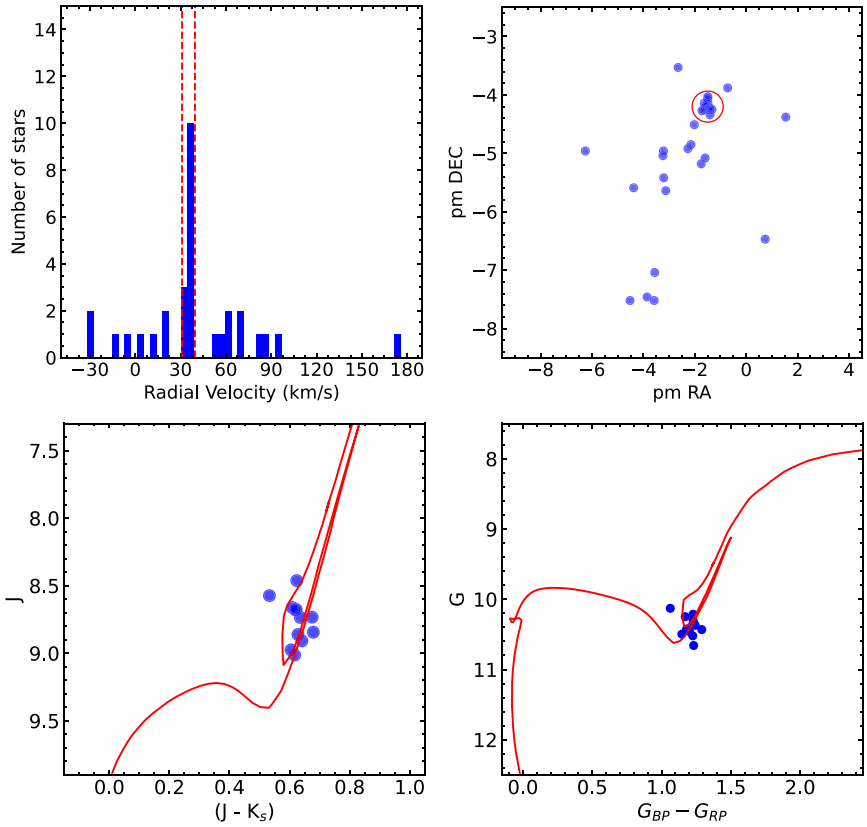

Figure 2. The upper left-hand panel displays the radial velocity distribution of stars in the 027–04 field, sourced from APOGEE DR17. The red dashed lines correspond to the radial velocity range determined for the cluster. In the upper right-hand panel, the *Gaia* DR3 proper motions of the targeted stars are presented. The blue dots inside the red circle signify stars within the radial velocity range determined for the cluster. The bottom panels depict the 2MASS ($J - K_s$) versuss J and *Gaia* DR2 ($G_{BP} - G_{RP}$) versus G diagrams. The red line in both cases represents the isochrones from Bressan et al. (2012).

Table 1. Member stars of NGC 6705.

Star ID	J (mag)	H (mag)	K (mag)	V (mag)	G (mag)	G_{BP} (mag)	G_{RP} (mag)	RV (km s^{-1})	SNR
2M18505494-0616182	9.199	8.498	8.318	11.860	11.338	12.131	10.467	35.019 ± 0.059	400
2M18510399-0620414	9.090	8.400	8.252	11.872	11.313	12.164	10.411	34.623 ± 0.018	467
2M18510661-0612442	9.035	8.406	8.213	11.720	11.184	11.997	10.306	33.761 ± 0.047	462
2M18511048-0615470	8.817	8.224	7.991	11.627	11.095	11.905	10.214	33.597 ± 0.019	488
2M18505944-0612435	9.330	8.722	8.523	11.872	11.378	12.138	10.528	34.710 ± 0.022	385
2M18510032-0617183	9.368	8.751	8.549	12.081	11.540	12.347	10.652	36.689 ± 0.050	396
2M18510341-0616202	9.216	8.579	8.386	11.801	11.305	12.087	10.443	37.108 ± 0.007	429
2M18510786-0617119	9.030	8.399	8.206	11.621	11.129	11.905	10.271	34.572 ± 0.019	359
2M18511452-0616551	9.263	8.620	8.420	11.923	11.402	12.209	10.521	36.307 ± 0.045	306
2M18510092-0614564	9.016	8.395	8.205	11.484	11.010	11.716	10.189	34.827 ± 0.509	466
2M18510626-0615134	8.928	8.379	8.193	11.627	11.222	12.030	10.337	35.116 ± 0.007	449
2M18511571-0618146	9.088	8.445	8.211	11.807	11.252	12.073	10.367	35.442 ± 0.024	475

the effective temperatures determined from each colour and the corresponding median effective temperatures (and median absolute deviation, MAD). The effective temperatures obtained from different colours agree quite well, with the MAD for most stars being less than 50 K, which is a typical uncertainty for effective temperature scales. We note also that these errors are similar to those found in Souto et al. (2016) for a sample of red-giants in the open cluster NGC 2420.

To determine the surface gravities for the targets, the fundamental relation (equation (2)) was used, with the following reference solar parameter values: log g = 4.438 (cgs), $T_{\rm eff,\odot}$ = 5770 K, and a bolometric magnitude of $M_{\rm bol,\odot}$ = 4.75 (Prša et al. 2016). The effective temperatures used are the median effective temperatures listed in Table 2. Stellar masses were derived using the PARSEC isochrones (Bressan et al. 2012), which yield a mass of ∼3.3 $M_\odot$ for a cluster age of 0.316 Gyr (Cantat-Gaudin et al. 2018) and a metallicity of $[M/H] = +0.10$ dex. Absolute magnitudes were determined using the distance module $(m\text{-}M)_o = 11.38$ (Dias et al. 2021), along with bolometric corrections from Montegriffo et al. (1998):

$$\log g = \log g_\odot + \log\left(\frac{M_\star}{M_\odot}\right) + 4\log\left(\frac{T_\star}{T_\odot}\right) + 0.4(M_{\rm bol,\star} - M_{\rm bol,\odot}). \quad (2)$$

Table 2. Atmospheric parameters.

Star ID	$T_{\rm eff}(V-J)$ (K)	$T_{\rm eff}(V-H)$ (K)	$T_{\rm eff}\,(V-K_s)$ (K)	$T_{\rm eff}\,(J-K_s)$ (K)	$\langle T_{\rm eff}\rangle$ (K)	log g (cm s^{-2})	[Fe/H] (dex)	ξ (km s^{-1})
2M18505494-0616182	4735	4692	4715	4632	4704 ± 31	2.279	0.15	1.50
2M18510399-0620414	4599	4601	4651	4754	4626 ± 51	2.253	0.07	1.70
2M18510661-0612442	4707	4734	4745	4801	4739 ± 27	2.250	0.14	1.80
2M18511048-0615470	4570	4658	4638	4789	4648 ± 63	2.167	0.12	1.60
2M18505944-0612435	4882	4884	4885	4846	4883 ± 14	2.386	0.16	1.60
2M18510032-0617183	4675	4720	4723	4810	4722 ± 39	2.359	0.03	1.70
2M18510341-0616202	4827	4816	4825	4778	4821 ± 17	2.334	0.15	1.75
2M18510786-0617119	4819	4816	4825	4795	4818 ± 9	2.272	0.17	1.90
2M18511452-0616551	4736	4744	4748	4740	4742 ± 4	2.318	0.15	1.70
2M18510626-0615134	4691	4793	4808	5073	4800 ± 116	2.304	0.16	1.80
2M18511571-0618146	4668	4692	4670	4643	4669 ± 13	2.263	0.18	1.50

Table 3. Mean abundance differences of Na, Mg, K, and Ca (with STD) in Non-LTE and LTE.

Element	$\langle\delta[X/H]\rangle$ (non-LTE–LTE)
Na	-0.019 ± 0.003
Mg	-0.027 ± 0.006
K	$+0.007 \pm 0.010$
Ca	-0.032 ± 0.010

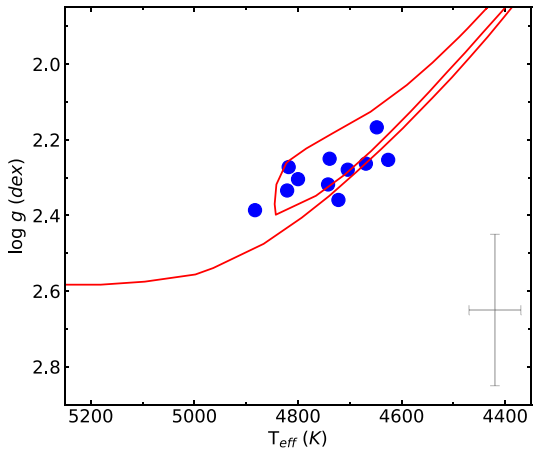

Figure 3. Kiel diagram. The red line in the plot represents the isochrone for metallicity of [Fe/H] = 0.13 dex and age of 0.316 Gyr. The isochrone was calculated using PARSEC (Bressan et al. 2012). Effective temperatures and surface gravities are the values determined in this work (see Table 2). A typical errorbar is shown in the bottom right of the figure.

The stellar parameters of our sample are presented in Fig. 3 as a Kiel diagram, where we also show as a red line a PARSEC isochrone (Bressan et al. 2012) computed for a metallicity of 0.13 dex and an age of 0.316 Gyr. The studied stars occupy a small range in parameter space close to the red clump, with the effective temperatures ranging between ∼4600–4900 K and surface gravities spanning from 2.2 to 2.4 dex. In Fig. 3, the stellar parameters seem to segregate, with four targets being hotter than 4800 K and more in line with them being on the red clump and seven targets cooler than 4800 K and falling closer to the RGB branch. However, given the uncertainties both in the stellar parameters and in the models, a secure distinction between red clump and RGB is difficult to make since we do not have information from asteroseismology.

4 ABUNDANCE ANALYSES AND METHODOLOGY

The chemical abundances for seventeen elements were calculated by comparing observed and synthetic spectra through the χ^2-fitting method. Synthetic spectra were generated using MARCS model atmospheres (Gustafsson et al. 2008) and the Brussels Automatic Code for Characterizing High Accuracy Spectra (BACCHUS; Masseron, Merle & Hawkins 2016), which utilizes the radiative transfer code Turbospectrum (Alvarez & Plez 1998; Plez 2012). The APOGEE line list was adopted in the calculations of synthetic spectra (Smith et al. 2021).

We derived the stellar metallicities and microturbulent velocities using nine Fe I lines selected in the APOGEE region by Smith et al. (2013) and the methodology discussed in Souto et al. (2016). Briefly, the methodology consists of measuring the iron abundance of each Fe I line for different values of microturbulent velocities (ξ) using the spectrum synthesis method. The adopted values of microturbulent velocities were the ones that produced the smallest spread between the iron abundances of the individual lines.

The APOGEE spectra of red giant stars are characterized by the presence of numerous molecular features, predominantly spectral lines from CO, CN, and OH, making it an ideal tool for accurately determining the abundances of carbon, nitrogen, and oxygen. The molecular lines used for abundance determination are $^{12}C^{16}O$, $^{12}C^{14}N$, and ^{16}OH, respectively, with the procedure to determine the C, N, and O abundances following the Smith et al. (2013) methodology. First, we derive the abundance of carbon from the molecular CO lines, then the oxygen abundance from the OH lines, and lastly, the nitrogen abundance from the CN lines.

The spectral range covered by APOGEE also contains atomic lines from many elements, including α-elements, such as Mg, Si, Ca, and Ti, along with odd-Z elements, such as, Na, Al, and K, as well as the Fe-peak elements V, Cr, Mn, Fe, Co, and Ni, and the s-process element Ce. In this analysis, we analysed 73 spectral features that had been selected in the previous APOGEE studies of red giants of Smith et al. (2013), Cunha et al. (2015), and Souto et al. (2016) as abundance indicators: 9 Fe I lines, 4 CO lines, 9 CN lines, 2 Na I lines, 6 Mg I lines, 2 Al I lines, 7 Si I lines, 2 K I lines, 3 Ca I lines, 5 Ti I lines, 1 V I line, 1 Cr I line, 3 Mn lines, 1 Co I line, 7 Ni I lines, 7 Ce II lines, and 4 OH lines, noting that the latter are blended with CN at the studied range in parameter space. Table 4 contains the atomic and molecular line list used in the abundance analysis, the corresponding line-by-line abundances, the mean abundances, and standard deviations for each star, while in Table 5, we list the mean abundances, and standard deviation (STD) obtained for the

Table 4. Line-by-line elemental abundances.

Element	λ (Å)	J18505494 −616182	J18510399 −620414	J18510661 −612442	J18511048 −615470	J18505944 −612435	J18510032 −617183	J18510341 −616202	J18510786 −617119	J18511452 −616551	J18510626 −615134	J18511571 −618146
C from CO	15580.	8.42	8.33	8.41	8.45	8.51	8.33	8.49	8.51	8.43	8.45	8.43
	15977.	8.48	8.29	8.46	8.33	8.45	8.24	8.44	8.55	8.39	8.40	8.44
	16186.	8.47	8.35	8.55	8.42	8.54	8.32	8.51	8.60	...	8.44	8.48
	16613.	8.51	8.33	8.47	8.39	8.50	8.31	8.50	8.51	8.45	8.49	8.48
⟨*A*(C)⟩		8.47 ± 0.03	8.32 ± 0.02	8.47 ± 0.05	8.40 ± 0.04	8.50 ± 0.03	8.30 ± 0.04	8.48 ± 0.03	8.54 ± 0.04	8.42 ± 0.02	8.45 ± 0.03	8.46 ± 0.02
N from CN	15260.	8.43	8.59	8.50	8.52	8.46	8.49	8.49	8.46	8.43	8.52	8.40
	15322.	8.47	8.60	8.49	8.56	8.50	8.46	8.53	8.53	8.49	8.53	8.39
	15397.	8.60	8.63	8.59	8.51	8.58	8.50	8.59	8.69	8.50	8.51	8.42
	15332.	8.50	8.54	8.49	8.56	8.55	8.57	8.55	8.54	8.49	8.53	8.45
	15410.	8.41	8.58	8.42	8.42	8.46	8.46	8.46	8.49	8.45	8.52	8.37
	15447.	8.42	8.63	8.48	8.55	8.53	8.51	8.52	8.55	8.56	8.52	8.48
	15466.	...	...	8.28	8.40	8.42	...	8.41	8.42	8.37	8.41	8.27
	15472.	8.29	8.47	8.33	8.35	8.34	8.40	...	...	8.26	8.43	8.30
	15482.	8.36	8.52	8.38	8.40	8.45	8.39	8.48	8.46	8.33	8.50	8.33
⟨*A*(N)⟩		8.43 ± 0.09	8.57 ± 0.05	8.44 ± 0.09	8.47 ± 0.08	8.48 ± 0.07	8.47 ± 0.05	8.50 ± 0.05	8.52 ± 0.08	8.43 ± 0.09	8.50 ± 0.04	8.38 ± 0.07
O from OH	15280.	...	8.77	8.78	8.73	8.81	...	8.86	...	...	... 8.83	
	15505.	8.80	8.85	8.57	8.65	8.65	8.77	8.70	8.76	8.72	8.69	8.78
	15570.	...	...	...	8.87	...	...	...	...	...	...	...
	16191.	...	8.71	8.75	8.68	8.77	...	8.81	8.85	...	8.85	8.69
⟨*A*(O)⟩		8.80	8.78 ± 0.06	8.70 ± 0.09	8.73 ± 0.08	8.75 ± 0.07	8.77	8.79 ± 0.07	8.80 ± 0.05	8.72	8.77 ± 0.08	8.77 ± 0.06
Fe I	15194.492	7.72	7.50	7.69	7.61	...	7.50	7.72	...	7.67	7.75	7.64
	15207.526	7.58	...	7.43	7.40	...	...	...	...	7.47	7.60	...
	15395.718	7.64	7.51	7.62	7.64	7.59	7.52	7.49	7.58	7.66	7.64	7.71
	15490.339	7.65	7.53	7.61	7.53	7.50	7.42	7.59	7.54	7.53	7.58	7.61
	15648.51	7.64	7.69	7.65	7.63	7.73	7.56	7.69	7.59	7.69	7.64	7.65
	15964.867	7.50	7.42	7.62	7.58	7.56	7.48	7.63	7.65	7.60	7.60	7.65
	16040.657	7.54	7.46	7.54	7.56	7.58	7.46	7.48	7.62	7.52	7.55	7.56
	16153.247	7.53	7.49	7.52	7.60	7.61	7.45	7.54	7.68	...	7.55	7.54
	16165.032	7.71	7.62	7.71	7.72	7.78	...	7.71	7.72	7.77	7.65	7.76
⟨*A*(Fe)⟩		7.61 ± 0.07	7.53 ± 0.08	7.60 ± 0.08	7.58 ± 0.08	7.62 ± 0.09	7.49 ± 0.04	7.61 ± 0.09	7.63 ± 0.06	7.61 ± 0.10	7.62 ± 0.06	7.64 ± 0.07
Na I	16373.853	6.67	6.67	6.62	6.55	6.65	6.49	6.60	6.67	6.64	6.61	6.62
	16388.858	6.74	6.73	6.66	6.62	6.72	6.55	6.65	...	6.67	6.72	6.67
⟨*A*(Na)⟩		6.71 ± 0.04	6.70 ± 0.03	6.64 ± 0.02	6.59 ± 0.04	6.68 ± 0.03	6.52 ± 0.03	6.63 ± 0.03	6.67	6.66 ± 0.02	6.67 ± 0.05	6.65 ± 0.03
Mg I	15740.716	7.75	7.60	7.67	7.61	7.72	7.51	7.63	7.63	7.70	7.57	7.68
	15748.9	7.72	7.63	7.63	7.52	7.65	7.51	...	7.61	7.57	7.55	7.68
	15765.8	7.69	7.60	7.69	7.60	7.77	7.60	7.70	7.76	7.70	7.50	7.59
	15879.5	7.55	7.74	7.58	7.55	7.54	7.68	7.56	7.60	7.75	7.54	7.78
	15886.2	7.80	7.81	7.84	7.78	...	7.78	...	...	7.86	7.73	7.82
	15954.477	7.71	7.72	7.75	7.68	7.77	7.63	...	7.67	7.74	7.59	7.66
⟨*A* (Mg)⟩		7.70 ± 0.08	7.68 ± 0.08	7.69 ± 0.08	7.62 ± 0.09	7.69 ± 0.09	7.62 ± 0.10	7.63 ± 0.06	7.65 ± 0.06	7.72 ± 0.09	7.58 ± 0.07	7.70 ± 0.07
Al I	16718.957	6.77	6.58	6.76	6.62	...	6.53	6.70	6.68	6.71	6.65	6.72
	16763.359	6.72	6.58	6.66	6.50	6.49	6.45	6.60	6.55	6.65	6.61	6.64
⟨*A*(Al)⟩		6.75 ± 0.02	6.58 ± 0.00	6.71 ± 0.05	6.56 ± 0.06	6.49	6.49 ± 0.04	6.65 ± 0.05	6.61 ± 0.06	6.68 ± 0.03	6.63 ± 0.02	6.68 ± 0.04
Si I	15361.161	7.68	7.75	7.78	7.75	7.68	7.73	7.59	7.58	7.78	7.74	7.80
	15376.831	7.89	7.83	7.83	7.85	7.80	7.75	7.84	7.78	7.86	7.87	7.92

Table 4 – *continued*

Element	λ (Å)	J18505494 −616182	J18510399 −620414	J18510661 −612442	J18511048 −615470	J18505944 −612435	J18510032 −617183	J18510341 −616202	J18510786 −617119	J18511452 −616551	J18510626 −615134	J18511571 −618146
	16060.009	7.56	7.48	7.45	7.45	7.56	7.45	7.47	7.44	7.57	7.50	7.61
	16094.787	7.79	7.60	7.71	7.61	7.68	7.48	7.63	7.70	7.76	7.80	7.85
	16215.67	7.73	7.52	7.71	7.58	7.64	7.48	7.60	7.73	7.74	7.60	7.67
	16680.77	7.70	7.63	7.78	7.61	7.73	7.55	7.63	7.73	7.77	7.70	7.73
	16828.159	...	7.61	7.78	7.61	7.65	7.52	7.55	7.65	7.75	7.61	7.67
⟨*A*(Si)⟩		7.73 ± 0.10	7.63 ± 0.11	7.72 ± 0.12	7.64 ± 0.12	7.68 ± 0.07	7.57 ± 0.11	7.62 ± 0.10	7.66 ± 0.11	7.75 ± 0.08	7.69 ± 0.12	7.75 ± 0.10
K I	15163.07	5.04	5.10	5.08	4.92	4.81	5.01	4.84	4.87	...	5.07	5.10
	15168.38	5.04	5.04	5.03	4.88	4.90	5.01	4.95	4.90	4.95	4.93	5.04
⟨*A*(K)⟩		5.04 ± 0.00	5.07 ± 0.03	5.06 ± 0.02	4.90 ± 0.02	4.86 ± 0.05	5.01 ± 0.00	4.90 ± 0.06	4.89 ± 0.02	4.95	5.00 ± 0.07	5.07 ± 0.03
Ca I	16150.763	6.55	6.33	6.43	6.42	6.47	6.30	6.40	6.50	6.57	6.42	6.39
	16155.236	6.61	6.40	6.52	6.45	6.51	6.36	6.50	6.51	6.59	6.50	6.45
	16157.364	...	6.36	6.47	6.38	6.50	6.38	6.45	6.45	6.58	6.50	6.47
⟨*A*(Ca)⟩		6.58 ± 0.03	6.36 ± 0.03	6.47 ± 0.04	6.42 ± 0.03	6.49 ± 0.02	6.35 ± 0.03	6.45 ± 0.04	6.49 ± 0.03	6.58 ± 0.01	6.47 ± 0.04	6.44 ± 0.03
Ti I	15543.756	5.22	4.92	5.01	4.90	5.09	4.77	4.98	5.09	5.08	5.11	5.04
	15602.842	5.28	5.02	5.17	4.94	5.23	5.01	5.20	5.25	5.14	5.28	5.13
	15698.979	5.16	4.94	5.03	4.80	4.98	4.79	4.92	...	5.13	4.95	5.08
	15715.573	5.09	4.83	...	4.68	4.96	4.75	4.92	4.92	4.88	4.95	4.95
	16635.161	5.19	...	...	4.83	4.84	...	...	...	4.92	...	4.93
⟨*A*(Ti)⟩		5.19 ± 0.06	4.93 ± 0.07	5.07 ± 0.07	4.83 ± 0.09	5.02 ± 0.13	4.83 ± 0.10	5.01 ± 0.12	5.03 ± 0.13	5.03 ± 0.11	5.07 ± 0.14	5.03 ± 0.08
V I	5924.769	4.08	4.01	4.15	3.98	4.10	4.11	4.19	4.10	4.13	4.09	4.00
⟨*A*(V)⟩		4.08	4.01	4.15	3.98	4.10	4.11	4.19	4.10	4.13	4.09	4.00
Cr I	15680.063	5.94	5.76	5.76	5.62	5.86	5.69	5.67	5.71	5.85	5.74	5.78
⟨*A*(Cr)⟩		5.94	5.76	5.76	5.62	5.86	5.69	5.67	5.71	5.85	5.74	5.78
Mn I	15159.	5.70	5.68	5.65	5.56	5.50	5.56	5.63	5.60	5.61	5.64	5.58
	15217.	5.55	...	5.48	5.35	5.42	5.33	5.40	5.43	5.45	5.56	5.47
	15262.	5.70	5.59	5.67	5.50	5.55	5.48	5.53	5.50	5.61	5.68	5.70
⟨*A*(Mn)⟩		5.65 ± 0.07	5.63 ± 0.04	5.60 ± 0.08	5.47 ± 0.09	5.49 ± 0.05	5.46 ± 0.09	5.52 ± 0.09	5.51 ± 0.07	5.56 ± 0.07	5.63 ± 0.05	5.58 ± 0.09
Co I	16757.7	5.11	5.06	5.12	4.94	5.10	4.97	5.08	5.15	5.07	5.07	5.04
⟨*A*(Co)⟩		5.11	5.06	5.12	4.94	5.10	4.97	5.08	5.15	5.07	5.07	5.04
Ni I	15605.68	6.58	6.42	6.50	6.36	6.43	6.34	6.40	6.40	6.49	6.41	6.50
	15632.654	6.56	6.38	6.45	6.41	6.48	6.30	6.42	6.45	6.54	6.39	6.52
	16584.44	6.56	6.39	6.50	6.45	6.49	6.44	6.57	6.48	6.59	6.42	6.49
	16589.30	6.43	6.34	6.51	6.41	6.36	6.37	6.47	6.31	6.51	6.47	6.46
	16673.711	...	6.28	6.30	6.37	6.27	6.30	6.37	6.31	6.32	6.35	6.29
	16815.471	6.51	6.46	6.40	6.28	6.37	6.39	6.40	6.37	6.32	6.51	6.43
	16818.76	...	6.54	6.58	6.43	6.51	6.52	6.48	6.34	6.56	...	6.55
⟨*A*(Ni)⟩		6.53 ± 0.05	6.40 ± 0.08	6.46 ± 0.08	6.39 ± 0.05	6.41 ± 0.08	6.38 ± 0.07	6.45 ± 0.06	6.38 ± 0.06	6.48 ± 0.10	6.43 ± 0.05	6.46 ± 0.08
Ce II	15784.786	1.86	1.79	1.72	1.79	1.82	1.82	1.80	...	1.82	1.84	1.79
	15958.39	1.90	...	...	1.89	...	1.84	...	2.05	...	1.72	1.87
	15977.12	1.83	...	1.81	...	...	...	...	...	1.75	1.72	...
	16327.32	...	...	...	...	...	...	1.70	...	...	...	...
	16376.46	1.78	1.91	1.91	1.85	1.93	1.80	1.80	1.90	...	...	1.96
	16595.233	1.97	1.75	1.82	...	1.84	...	1.77	1.92	1.74	1.90	1.69
	16722.6	...	1.98	...	2.03	1.96	1.92	...	2.06	...	...	2.00
⟨*A*(Ce)⟩	–	1.87 ± 0.06	1.86 ± 0.09	1.81 ± 0.07	1.89 ± 0.09	1.89 ± 0.06	1.84 ± 0.05	1.77 ± 0.04	1.98 ± 0.07	1.77 ± 0.04	1.80 ± 0.08	1.86 ± 0.11

Table 5. Mean NGC 6705 abundances.

Element	$\langle A(X)\rangle$	$\langle [X/H]\rangle$	STD	$\sigma(X)$
C	8.44	−0.02	0.07	0.057
N	8.47	0.64	0.05	0.085
O	8.76	0.07	0.03	0.132
Fe	7.59	0.13	0.04	0.035
Na	6.65	0.43	0.05	0.035
Mg	7.66	0.11	0.04	0.078
Al	6.62	0.19	0.08	0.055
Si	7.68	0.17	0.06	0.055
K	4.98	−0.09	0.08	0.053
Ca	6.46	0.16	0.07	0.058
Ti	5.01	0.04	0.10	0.103
V	4.06	0.19	0.06	0.051
Cr	5.76	0.14	0.09	0.032
Mn	5.55	0.13	0.07	0.062
Co	5.06	0.12	0.06	0.067
Ni	6.43	0.23	0.05	0.044
Ce	1.85	0.27	0.06	0.101

cluster, along with mean [X/H] ratios relative to the Solar abundances (Asplund, Amarsi & Grevesse 2021).

4.1 Abundance sensitivities and uncertainties

Souto et al. (2016, their table 4) estimated abundance uncertainties due to changes in stellar parameters), σ, for all elements analysed here, except for Ce. The uncertainties were computed by using the quadrature sum of abundance changes obtained by varying, respectively, the effective temperature by +50 K, the surface gravity by +0.2 dex, the metallicity by +0.2 dex, and the microturbulent velocity by +0.2 km s^{-1} (see also the discussion in, Smith et al. 2013; Souto et al. 2016). Here, we add the uncertainties calculated for cerium: the change in the Ce abundance due to a +50 K variation in $T_{\rm eff}$ is +0.06 dex, while for Δlog g of +0.2 it is +0.06 dex, for $\Delta\xi$ of +0.2 km s^{-1} it is −0.04 dex, and for Δ[M/H] of +0.2 dex is +0.04 dex. Summing these abundance changes in quadrature, we obtain an uncertainty in the Ce abundance of 0.1 dex. Table 5 (last column) lists these estimated uncertainties for all elements.

The elemental abundances in this study were derived, in general (except for V, Cr, and Co), from more than one atomic or molecular line, with the spread in the individual line abundances for a given star used to evaluate the internal consistency between the different line measurements. The STDs of the mean abundances in Table 4 are, for some elements quite small, being less than 0.04–0.05 dex, such as for C and Ca, while for many of the elements it is ∼0.09–0.1 dex, such as for O, N, Al, Fe, and Mg, while, in a few cases, the STDs of the mean reach values of 0.12–0.15 dex in some stars, such as for Si, Ti, and Ce.

Finally, given that the members of NGC 6705 presumably formed as a single stellar population, and that they are not affected by diffusion effects as they are on RGB or red clump (Bertelli Motta et al. 2018; Gao et al. 2018; Souto et al. 2018), one can use the STDs of the mean elemental abundances in the cluster (Table 5) to also gauge internal uncertainties in the analysis. The elements with the smallest abundance scatter among the member stars analysed (STD ≤ 0.05 dex) are O, N, Na, Mg, Fe, and Ni. The elements C, Al, Si, K, Ca, V, Mn, Co, and Ce exhibit higher scatter, although still moderate, ranging from 0.06 to 0.08 dex. For Cr, the scatter is 0.09 dex (which can be related to the fact that this element has only one measurable weak line in the APOGEE window), while for Ti, we find a scatter of 0.10 dex. We note that the STD for the iron abundances (0.04 dex), for example, is comparable to that reported by Cunha et al. (2015) for the open cluster NGC 6791, and Souto et al. (2016) for NGC 2420, both of which used APOGEE spectra of red giants in their analyses.

4.2 Non-LTE corrections for Na, Mg, K, and Ca

Non-LTE corrections to the LTE Na, Mg, K, and Ca abundances derived in this study can be estimated from the LTE and non-LTE abundances taken from spectral libraries generated for APOGEE DR17. Such synthetic spectra were computed using the Synspec spectral synthesis code (Hubeny et al. 2021), the APOGEE line list (Smith et al. 2021), APOGEE MARCS models (Gustafsson et al. 2008), and in the case of non-LTE, adopting atomic models for Na, Mg, K, and Ca discussed in Osorio et al. (2020). Both the LTE and non-LTE abundances were calculated using the ASPCAP pipeline (García Pérez et al. 2016). The mean differences between the non-LTE and LTE abundance results for our sample stars are given in Table 3.

The mean abundance differences 'non-LTE–LTE' are quite small for all four elements. For sodium, magnesium, and calcium the corrections were found to be negative, indicating that the LTE abundances of these elements are slightly overestimated, but not significantly so, relative to the non-LTE abundances by −0.02, −0.03, and −0.03, respectively. The mean difference for potassium is positive but also insignificant, at +0.01. It's worth noting that these differences are within the uncertainties associated with the abundances of these elements (see Table 5) and non-LTE corrected abundances will not be considered in this study.

5 COMPARISONS WITH PREVIOUS RESULTS

5.1 Stellar parameters

As discussed previously, the derived stellar parameters in this study relied on photometric calibrations for the derivation of the effective temperature, and fundamental relations for the derivation of the surface gravity. In the following, we compare our parameters with those obtained from high-resolution spectroscopy in the literature.

Several of the more recent studies of the open cluster NGC 6705 presented results from the GES, such as Cantat-Gaudin et al. (2014, 25 stars), Tautvaišienė et al. (2015, 27 stars), Magrini et al. (2017, 15 stars), and Magrini et al. (2021, 71 stars), who used effective temperatures and surface gravities from different survey data releases: GES-viDR1-final, GESviDR2Final, GES-IDR4, and GES-iDR6, respectively. In addition to these studies, there are also results for the NGC 6705 stars studied here in GES-DR5 (latest data release). Another recent study in the literature by Casamiquela et al. (2018) analysed eight stellar members of NGC 6705 observed by the OCCASO survey (Casamiquela et al. 2016).

A comparison of the effective temperatures for stars in common between our work and the studies mentioned above is shown in the top left-hand panel of Fig. 4, while the top right-hand panel shows the ASPCAP pipeline (García Pérez et al. 2016) results from APOGEE DR17 and GES-DR5: residual differences as a function of the literature $T_{\rm eff}$ are shown at the bottom of the two panels. The median differences between the effective temperatures in 'This work – Others' (±MAD) are as follows: −42 ± 57 K for Cantat-Gaudin et al. (2014) (9 stars); 6 ± 41 K for Tautvaišienė et al. (2015) (10 stars); 29 ± 33 K for Magrini et al. (2017) (5 stars); −69 ± 14 K for Casamiquela et al. (2018) (3 stars); 57.5 ± 34.0 for Magrini et al. (2021) (8 stars). The comparison with results GES-DR5 finds $<\Delta T_{\rm eff}>$ = 61 ± 34 K (10 stars) and with ASPCAP APOGEE DR17 (uncalibrated) is 28 ± 55 K (11 stars). In general, all analyses

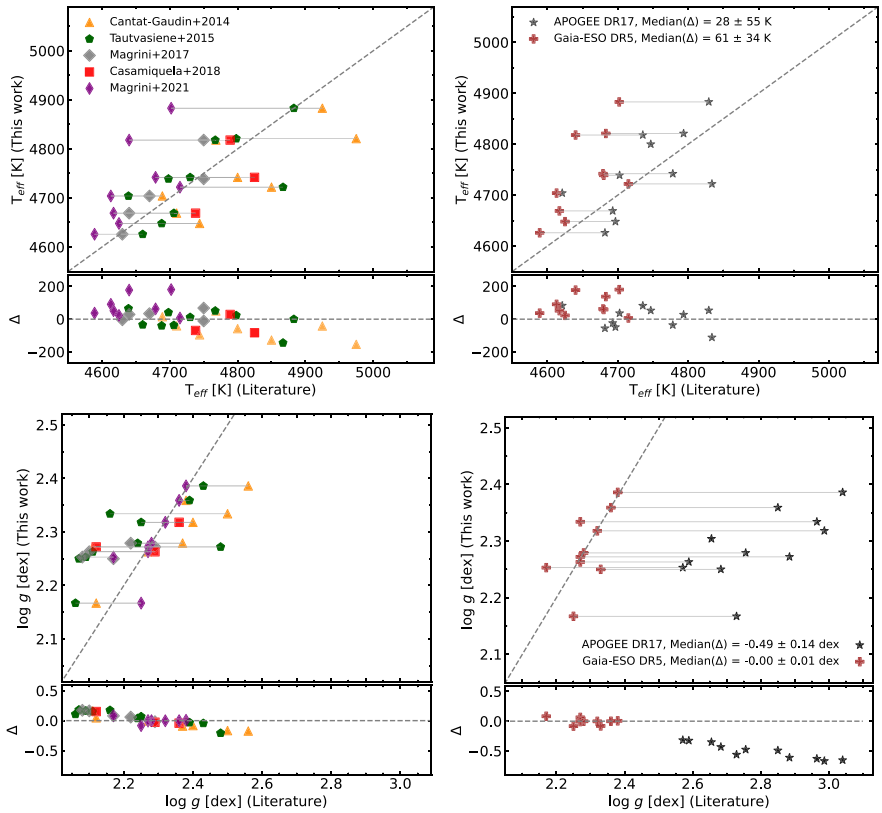

Figure 4. Comparison of the effective temperatures (top panels) and surface gravities (bottom panels) derived in this work with the literature results. The orange triangles show the comparison with Cantat-Gaudin et al. 2014, the green pentagons with Tautvaišienė et al. 2015, grey diamonds with Magrini et al. 2017, the red squares with Casamiquela et al. 2018, narrow purple diamonds with Magrini et al. 2021, black stars with APOGEE DR17 (non-calibrated), and the brown cross with GES DR5. Results for the same star are connected by the grey solid lines. The grey dashed lines represent equality. The lower panels show the differences, Δ, 'This work – Others' for effective temperatures and surface gravities, respectively.

yield consistent values of $T_{\rm eff}$ within typical uncertainties in effective temperature scales.

The two bottom panels of Fig. 4 are equivalent to the top panels, but the comparison is for surface gravities. The median differences (±MAD) in log g between 'This Work – Others' (left bottom panel) are, respectively: -0.06 ± 0.05 dex for (Cantat-Gaudin et al. 2014); 0.09 ± 0.08 dex for (Tautvaišienė et al. 2015), 0.08 ± 0.08 dex for (Magrini et al. 2017); and -0.03 ± 0.01 dex for (Casamiquela et al. 2018). Although there is overall good agreement in these median log g differences, which are well within the expected uncertainties for spectroscopically-determined values of log g (e.g. ∼0.2 dex), there are clear trends in the results, as can be seen from $\Delta\log g$ as a function of log g shown in the bottom subpanel. We generally find a smaller range in log g values for the comparison sample than in the literature. However, our log g values are in excellent agreement with GES-DR5: $\langle\Delta\log g\rangle = -0.0 \pm 0.01$ dex. APOGEE surface gravity results on the other hand, are known to have significant offsets (both for red giants and dwarfs) and this is clear from the bottom right-hand panel of Fig. 4. The range in log g from APOGEE DR17 (ASPCAP derived values) varies roughly between 2.6 and 3.1 dex and the median differences in log g values show systematics: -0.49 ± 0.14 dex. APOGEE also provides post-calibrated log g and in this case, the median log g differences are improved: -0.31 ± 0.14 dex.

5.2 Metallicities & other elemental abundances

There are several results for the metallicity of NGC 6705 in the literature. Metallicities derived spectroscopically, with values between +0.02 and +0.24 dex, are reported in studies by Gonzalez & Wallerstein (2000); Magrini et al. (2014); Tautvaišienė et al. (2015); Magrini et al. (2017); Casamiquela et al. (2018, 2021); Magrini et al. (2021). According to our results based on near-infrared spectroscopic analysis of a sample of eleven red giant stars, the mean metallicity of NGC 6705 is $\langle$[Fe/H]$\rangle = +0.13 \pm 0.04$ dex.

Fig. 5 shows violin distributions of the metallicity of NGC 6705 determined both in this study (white distribution) and other studies (grey distributions). The metallicity diagrams from this work, as well as Cantat-Gaudin et al. (2014), Tautvaišienė et al. (2015), Magrini et al. (2017), Casamiquela et al. (2018), and Magrini et al. (2021) are shown from top to bottom in chronological order. In general, our metallicity determination shows excellent agreement with Magrini et al. (2017) and Casamiquela et al. (2018) for their samples of 15 and 8 stars, with reported metallicities of [Fe/H] = $+0.12 \pm 0.05$ dex and [Fe/H] = $+0.17 \pm 0.04$ dex, respectively, or mean metallicity differences of +0.01 and −0.04 dex, respectively. However, the mean metallicity value determined here is somewhat larger than those reported by Tautvaišienė et al. (2015) in a sample of 27 stars ([Fe/H] = 0.00 ± 0.05 dex) and Magrini et al. (2021) using 71 stars (0.02 ± 0.05 dex), with the latter study having used both high-resolution UVES and lower resolution GIRAFFE data.

In addition, an investigation into the differences between the metallicities of 'This work – Other' (±MAD) for stars in common between the studies, finds good agreement in some cases and systematic differences in others. There are no significant systematic differences when comparing with Casamiquela et al. (2018), Magrini et al.

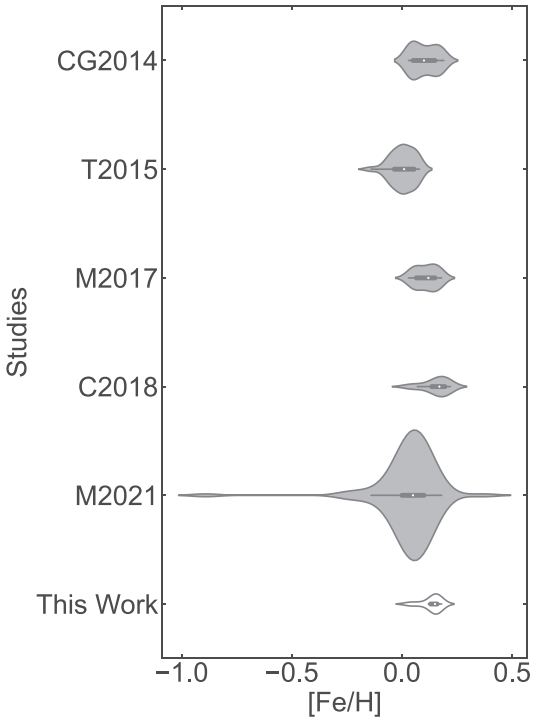

Figure 5. Metallicity distribution of NGC 6705 stars. The white distribution represents our [Fe/H] results, while the grey sequences show the literature [Fe/H] results: Cantat-Gaudin et al. (2014, CG2014), Tautvaišienė et al. (2015, T2015), Magrini et al. (2017, M2017), Casamiquela et al. (2018, C2018), and Magrini et al. (2021, M2021). White dots in the distribution indicate the median, while the thick bar represents the interquartile range, and the thin bar shows the 95 per cent confidence interval. Wider regions of the distribution represent a higher probability that a star will have that [Fe/H] value.

(2017), and Cantat-Gaudin et al. (2014), with median differences of 0.00 ± 0.01, 0.03 ± 0.02, and 0.03 ± 0.04 dex, respectively. The comparison with results from APOGEE DR17 is also very good: 0.04 ± 0.03 dex. On the other hand, there are larger differences between the metallicities of Tautvaišienė et al. (2015), Magrini et al. (2021), and GES DR5, for ten, eight and ten stars, with our metallicities being higher than theirs by 0.13 ± 0.04, 0.12 ± 0.04, and 0.12 ± 0.02 dex, respectively.

Besides metallicities, which are discussed above, we summarize in Table 6, the comparisons between the abundances of the other elements studied here with literature values, again exemplified as the median abundance differences (±MAD) [X/Fe] for 'This Work – Other Work' for stars in common with the studies of Cantat-Gaudin et al. (2014), Tautvaišienė et al. (2015), Magrini et al. (2017), Casamiquela et al. (2018), and the surveys APOGEE DR17 and GES-DR5. Most of the systematic differences between the results are less than or equal to 0.1 dex and this is not surprising given the different methodologies adopted in the various studies, but there are some cases with more significant discrepancies, such as, for example, oxygen having a median difference of −0.25 dex for Casamiquela et al. (2018) and −0.20 dex for GES-DR5, magnesium being different by −0.19 dex also for GES-DR5, or sodium having a −0.26 dex offset in comparison with Cantat-Gaudin et al. (2014). In addition, the MAD values for the majority of the cases are also typically small (<0.05 dex), with only one being larger than 0.1 dex.

6 DISCUSSION

6.1 C, N, O, Na, Al, and mixing in the red-giants of NGC 6705

NGC 6705 provides an important astrophysical laboratory in which to probe red-giant mixing in RGB and RC stars, as the masses of this cluster's red giants are $M \sim 3.3\,M_{\odot}$, well above the mass limit for stars that undergo the He-core flash ($M < 2.1\,M_{\odot}$ at solar metallicity, e.g. Karakas & Lattanzio 2014). As discussed in Section 3 and illustrated in Fig. 3, the red giants sampled here are likely a mixture of RGB and RC stars, with the interiors of the RGB stars consisting of an inert He core surrounded by a H-burning shell, while the RC stars have evolved beyond the RGB and are powered by core-He burning. Due to uncertainties in our derived values of $T_{\rm eff}$ and log g, assigning a classification to a red giant as either an RGB or RC star (without asteroseismic data) is uncertain, although based on their positions in the Kiel diagram in Fig. 3, it appears that those red giants with $T_{\rm eff} > 4750$–4800 K likely belong to the RC, while the cooler ones are evolving up the RGB. This classification criterion results in our sample dividing into four RC stars and seven RGB stars.

The luminosities of the RGB stars indicate that all have experienced the first dredge-up (as have the RC stars), which has contaminated their photospheres with matter that has undergone partial H-burning via the CN-cycle. This contamination is revealed through the abundances of carbon, both ^{12}C and ^{13}C (although carbon-13 will not be discussed here) and ^{14}N. As a result of the first dredge-up, the surface ^{12}C abundance will be lowered, while that of ^{14}N will be increased significantly. As shown in Table 5, the average carbon and nitrogen abundances are $\langle A(^{12}\mathrm{C})\rangle = 8.44 \pm 0.07$ and $\langle A(^{14}\mathrm{N})\rangle = 8.47 \pm 0.05$, respectively. The solar abundances are $A(^{12}\mathrm{C}) = 8.46$ and $A(^{14}\mathrm{N}) = 7.83$, but with the average metallicity of NGC 6705 being [Fe/H] = +0.13, the average cluster red giant abundances of carbon and nitrogen with respect to iron are $[^{12}\mathrm{C/Fe}] = -0.16$ and $[^{14}\mathrm{N/Fe}] = +0.51$, in qualitative agreement with that expected from first dredge-up. Theoretical models of the 1st dredge-up and thermohaline mixing by Charbonnel & Lagarde (2010) predict $[^{12}\mathrm{C/Fe}] = -0.21$ and $[^{14}\mathrm{N/Fe}] = +0.47$ for stars with $M = 3\,M_{\odot}$ after dredge-up, which is in quantitative agreement with our results for the red giants in NGC 6705.

Fig. 6 presents a different way to view the 1st dredge-up, with the ^{14}N-abundance plotted versus the ^{12}C-abundance, and the observed red giants in NGC 6705 are divided into RGB (blue symbols) and RC (red symbols) stars, respectively. The smooth magenta curve represents a constant sum of the number abundances of carbon-12 and nitrogen-14, as the sum of these nuclei are conserved approximately during CN-cycle H-burning. This curve represents schematically the 1st dredge-up as a mixing curve. There are four stable nuclei involved in the CN-cycle: ^{12}C, ^{13}C, ^{14}N, and ^{15}N, of which carbon-13 and nitrogen-15 are considered minor species. In pure equilibrium CN-cycle matter, the value of ^{12}C/^{13}C can be as small as 3.5, which would shift the upper part of the mixing curve in Fig. 6 to lower ^{12}C abundances by ∼0.1 dex, however, the expected ratio in 3.3 $M_{\odot}$ RGB stars is 18–20 (Lagarde et al. 2012; McCormick et al. 2023), which would have a negligible effect on the mixing curve. Nitrogen-15 is an even more minor species, with typical 1st dredge-up values expected to be smaller than the solar value of ^{14}N/^{15}N = 272 (Wannier et al. 1991), so this isotope can be neglected from our discussion.

The sum of N(^{12}C) + N(^{14}N) in Fig. 6 was taken as the average values from the RGB plus RC stars, and the initial individual carbon-12 and nitrogen-14 abundances were set assuming an initial solar ratio of N(C)/N(N) = 4.1 (Grevesse, Asplund & Sauval 2007). These two constraints lead to initial carbon and nitrogen abundances for

Table 6. Median abundance differences 'This Work – Other'.

[X/Fe]	APOGEE DR17 (#11)	GES DR5 (#10)	CG2014 (#8)	T2015 (#10)	M2017 (#5)	C2018 (#3)	SS2022 (#9)
C	−0.18 ± 0.03	−0.06 ± 0.04	...	−0.06 ± 0.03	...	...	...
N	0.06 ± 0.03	−0.05 ± 0.06	...	−0.12 ± 0.03	...	...	...
O	0.03 ± 0.02	−0.20 ± 0.03	...	−0.18 ± 0.08	−0.03 ± 0.04	−0.25 ± 0.07	...
Na	0.11 ± 0.05	0.03 ± 0.10	−0.26 ± 0.03	...	...	...	...
Mg	0.11 ± 0.03	−0.19 ± 0.06	−0.16 ± 0.04	...	−0.10 ± 0.04	−0.14 ± 0.11	...
Si	0.01 ± 0.03	−0.04 ± 0.07	0.03 ± 0.02	...	0.04 ± 0.04	−0.05 ± 0.06	...
Ca	0.04 ± 0.02	0.12 ± 0.09	...	...	0.11 ± 0.03	−0.05 ± 0.10	...
Al	−0.00 ± 0.04	−0.11 ± 0.05	−0.15 ± 0.06	...	...	...	...
K	−0.04 ± 0.06	...	...	...	...	...	...
Ti	−0.06 ± 0.05	−0.01 ± 0.10	...	...	0.05 ± 0.00	−0.11 ± 0.01	...
V	0.26 ± 0.03	0.05 ± 0.04	...	...	0.02 ± 0.01	...	...
Cr	0.03 ± 0.06	0.09 ± 0.10	...	...	0.15 ± 0.04	...	...
Mn	0.01 ± 0.06	0.07 ± 0.06	...	...	...	...	...
Co	−0.03 ± 0.04	−0.05 ± 0.05	...	...	...	...	...
Ni	0.10 ± 0.04	0.12 ± 0.05	...	...	0.12 ± 0.03	...	...
Ce	0.01 ± 0.07	0.05 ± 0.07	...	...	...	...	−0.07 ± 0.02

Note. Our results are compared with: CG2014: Cantat-Gaudin et al. (2014); T2015: Tautvaišienė et al. (2015); M2017: Magrini et al. (2017); C2018: Casamiquela et al. (2018); SS2022: and Sales-Silva et al. (2022).

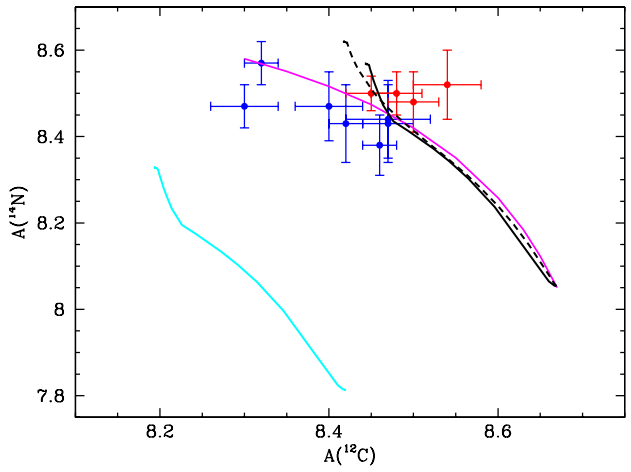

Figure 6. Carbon-12 and nitrogen-14 abundances for the NGC 6705 red giants are divided into RGB (blue symbols) and RC (red symbols) stars. The solid magenta curve is a 'mixing line' defined by a constant sum of ^{12}C and ^{14}N nuclei. A 3 $M_\odot$ solar-metallicity standard stellar model (i.e. no extra mixing) from Lagarde et al. (2012) is shown as a cyan curve, while the black curves represent solar metallicity models simply shifted by +0.22 dex in the initial ^{12}C and ^{14}N abundances to mimic the metallicity of NGC 6705, with the standard model shown by the solid line and a model that includes rotational and thermohaline mixing shown by the dashed line.

NGC 6705 of $A(^{12}C) = 8.67$ and $A(^{14}N) = 8.05$ and, with these initial abundance values, the mixing curve passes through the NGC 6705 RGB stars. One point to note from Fig. 6 is that the four RC stars, while having ^{14}N abundances that are very similar to the RGB stars, exhibit ^{12}C abundances that are slightly larger than the RGB sample. The average abundances of the two groups are $\langle A(^{12}C)\rangle = 8.41 \pm 0.07$ and $\langle A(^{14}N)\rangle = 8.46 \pm 0.05$ for the RGB stars and $\langle A(^{12}C)\rangle = 8.49 \pm 0.03$ and $\langle A(^{14}N)\rangle = 8.50 \pm 0.01$ for the RC stars, resulting in linear values for the C/N abundance ratios of 0.92 ± 0.22 and 0.99 ± 0.07 for the RGB and RC stars, respectively. A Kolmogorov–Smirnov test of the C/N ratios in the RGB and RC stars finds that they can be represented by a single population in C/N.

Models by Lagarde et al. (2012) for a 3 $M_\odot$ solar-metallicity star are also shown in Fig. 6 as a comparison to the simple mixing curve. As Lagarde et al. (2012) only presented solar-metallicity, or lower, models, we show their solar-metallicity model as the continuous cyan curve, which begins at an initial abundance of $A(^{12}C) = 8.43$ and $A(^{14}N) = 7.83$ and evolves from there. Since our discussion from above indicates that NGC 6705 is metal-rich relative to the Sun, the black curves in Fig. 6 represent solar-metallicity models from Lagarde et al. (2012) in which the initial ^{12}C and ^{14}N abundances are increased by +0.22 dex; the solid black curve is the standard model, while the dashed curve represents the model that includes rotational and thermohaline mixing. A quantitative comparison of models with observationally-derived abundance would demand consistent models; however, this straightforward test indicates that the 11 red giant members of NGC 6705 analysed here, at $M \sim 3.3\,M_\odot$, display unremarkable C and N abundances when compared to stellar models.

Moving up the periodic table past C and N, we investigate additional elemental abundances that are potentially sensitive to red giant mixing in the mass range of $M \sim 3$–$4\,M_\odot$ and focus on oxygen (as ^{16}O), sodium, and aluminum. The red giants studied here have a mass of $\sim$3.3 $M_\odot$ and exhibit a significant overabundance of [Na/Fe] = +0.29 ± 0.04 dex. This confirms that giant stars with masses greater than 3 $M_\odot$ can have an overabundance of sodium, providing a strong indication that the sodium overabundance in these stars is caused by internal evolutionary processes, as suggested by Smiljanic et al. (2016). More specifically, we examine the behaviours of [Na/Fe], [Al/Fe], and [O/Fe] as functions of stellar mass in Fig. 7 and, in addition to NGC 6705, we consider the slightly more metal poor ([Fe/H] = −0.16) open cluster NGC 2420 ($M_{TO} = 1.6\,M_\odot$) with Na, Al, and O abundances taken from Souto et al. (2016), the open clusters NGC 4815 ($M_{TO} = 2.5\,M_\odot$), Berkeley 81 ($M_{TO} = 2.2\,M_\odot$), and Trumpler 20 ($M_{TO} = 1.8\,M_\odot$), for which Na and Al abundances and masses were taken from Smiljanic et al. (2016), while the oxygen abundances are from Magrini et al. (2017); the models from Lagarde et al. (2012), both standard as well as those including rotation, are also shown. The left-hand panel of Fig. 7 reveals an overabundance of sodium which increases with increasing red-giant mass, as predicted by the models. In the case of Al (middle panel of Fig. 7), we observe that the mean Al abundance of NGC 6705

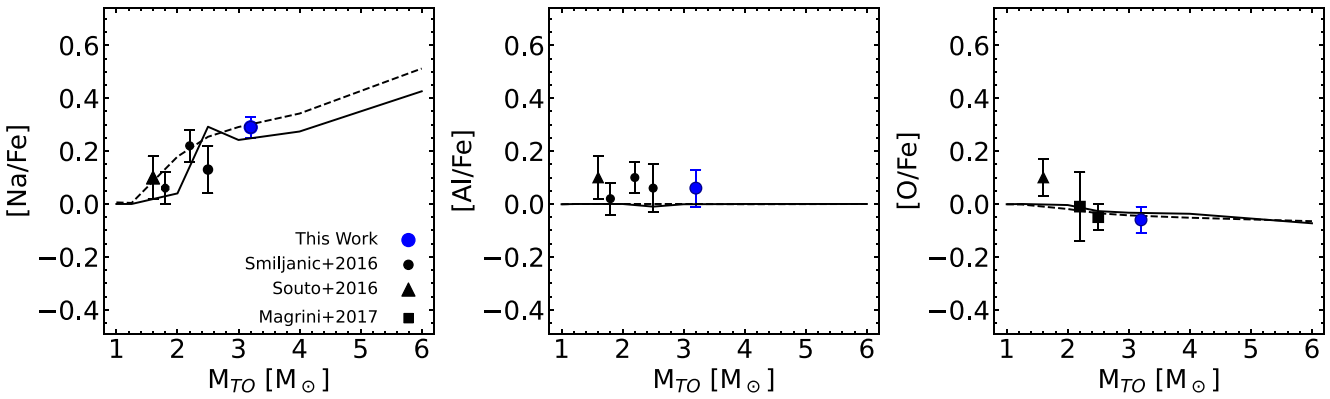

Figure 7. Mean cluster abundances of Na, Al, and O versus cluster turn-off mass. The blue circle corresponds to the abundances of NGC 6705 determined in this study, and the black circles correspond to mean Na and Al abundances of NGC 4815, Berkeley 81, and Trumpler 20 derived for giant stars in Smiljanic et al. (2016). Mean abundances of O are taken from Magrini et al. (2017) for NGC 4815 and Berkeley 81 (black squares). The black triangle correspond to mean Na, Al, and O abundances of NGC 2420 derived in Souto et al. (2016). The black solid and dashed lines correspond to the standard model and the model that includes rotational and thermohaline mixing, both from Lagarde et al. (2012), respectively.

determined here is slightly enhanced ([Al/Fe] $= +0.06 \pm 0.07$) but in agreement with the models within the uncertainties, with all clusters displaying a small (but not significant) offset from the models. In summary, we do not find that the [Al/Fe] abundance is enhanced in NGC 6705, unlike what was previously suggested in Smiljanic et al. (2016) for which the [Al/Fe] overabundance was +0.3. The right-hand panel of Fig. 7 shows [O/Fe] as a function of mass. According to the models of Lagarde et al. (2012), there is a small trend of decreasing oxygen with increasing stellar mass and our oxygen abundance for NGC 6705 is also in agreement with the models. Overall, the observed abundances of ^{12}C, ^{14}N, ^{16}O, Na, and Al in the NGC 6705 red giants provide a benchmark for models of red giant mixing in intermediate-mass stars of $M \sim 3$–4 $M_\odot$ at near-solar metallicity.

6.2 Is the young open cluster NGC 6705 α-enhanced?

As discussed in the introduction, one of the interesting recent results in the literature is the finding that there is a population of stars in the Galaxy that is young and enriched in [α/Fe]; a result which was based on stellar ages obtained via CoRoT asteroseismology and chemical abundances taken from the APOGEE survey (Chiappini et al. 2015). Martig et al. (2015) also identified young α-enhanced stars using independent age estimates inferred from Kepler asteroseismology. In simple terms, such population is unexpected because in principle a young star is formed from gas already enriched in Fe from SN Ia, having therefore a decreased [α/Fe] ratio. However, these α-enhanced stars that appear to be young may be products binary interactions/mergers (e.g. Izzard et al. 2018; Silva Aguirre et al. 2018; Hekker & Johnson 2019; Jofré et al. 2023), being actually old and having the expected α-Fe content for their age. Moreover, Miglio et al. (2021) identified a sample of 400 red giant stars from the Kepler field (having asteroseismic data) that belong to the thick disc ([α/Fe] $> +0.1$) and found that ∼5 per cent of stars on the RGB were overmassive given the estimated age of the thick disc stars of ∼11 Gyr ($M > 1.1$ $M_\odot$). This fraction of overmassive stars increased to ∼18 per cent for red clump giants and Miglio et al. (2021) suggest that this result supports the idea that these stars increased their initial masses via interactions with a binary companion (either mass transfer or mergers) while evolving up the RGB.

In this context, the results in the literature finding the members of the young open cluster NGC 6705 to be α-enhanced is puzzling. Casamiquela et al. (2018) studied a sample with eight stars members of the open cluster NGC 6705 from high-resolution optical spectra and found that they were enriched in α-elements with an average of $\langle$[α/Fe]$\rangle = +0.11 \pm 0.06$. Tautvaišienė et al. (2015) also studied NGC 6705 but focused only on the analysis of the elements carbon, nitrogen, and oxygen, which are involved in H-burning. They found that the mean oxygen abundance in their sample of 27 red giants was mildly enhanced, with $\langle$[O/Fe]$\rangle = 0.12 \pm 0.05$. Magrini et al. (2014, 2017) also found evidence of enhancements in some of the α-elements in this cluster. Such results for an open cluster provided a possible connection with the young and α-enhanced field stars in the Galaxy, which was examined in Casamiquela et al. (2018).

The main goal of this study was to do a detailed spectroscopic analysis of APOGEE spectra of NGC 6705 red-giants and, in particular, probe their α-element abundances. Fig. 8 summarizes our results in the form of the [α/Fe] versus [Fe/H] diagram for the five α-elements studied: O, Mg, Si, Ca, and Ti. Each panel depicts the mean [α/Fe] (represented by the red circles) and their corresponding STDs. The mean abundances obtained for the eleven studied red-giants are shown in each panel. On the solar scale, our sample exhibits on average a titanium-to-iron ratio ($\langle$[Ti/Fe]$\rangle = -0.10 \pm 0.08$), and an oxygen-to-iron ratio slightly below solar ($\langle$[O/Fe]$\rangle = -0.06 \pm 0.05$), while the mean calcium and silicon abundance ratios are marginally higher than solar scaled values, but not significantly so ($\langle$[Ca/Fe]$\rangle = +0.03 \pm 0.05$; $\langle$[Si/Fe]$\rangle = +0.03 \pm 0.04$). The magnesium abundance for the cluster is also not enhanced and has a mean value slightly below solar ($\langle$[Mg/Fe]$\rangle = -0.02 \pm 0.05$). All in all, our analysis does not find NGC 6705 to be α-enhanced and this is corroborated by the average of the four α-elements studied, which yields $\langle$[α/Fe]$\rangle = -0.03 \pm 0.05$.

Given the location of NGC 6705 in the inner Galactic disc, it is also of interest to investigate whether the measured [α/Fe] abundances for this open cluster are consistent with those of other open clusters residing in the inner galaxy, and how their α-element abundance pattern contrasts with the galactic abundance gradients. The mean Fe abundances obtained here for NGC 6705 are in line with the gradients for [Fe/H] versus R_{GC} presented in Fig. 4 of Myers et al. (2022). The five panels of Fig. 9 show the O, Mg, Si, Ca, and Ti over Fe ratios as a function of galactocentric distance (R_{GC}) for the open clusters

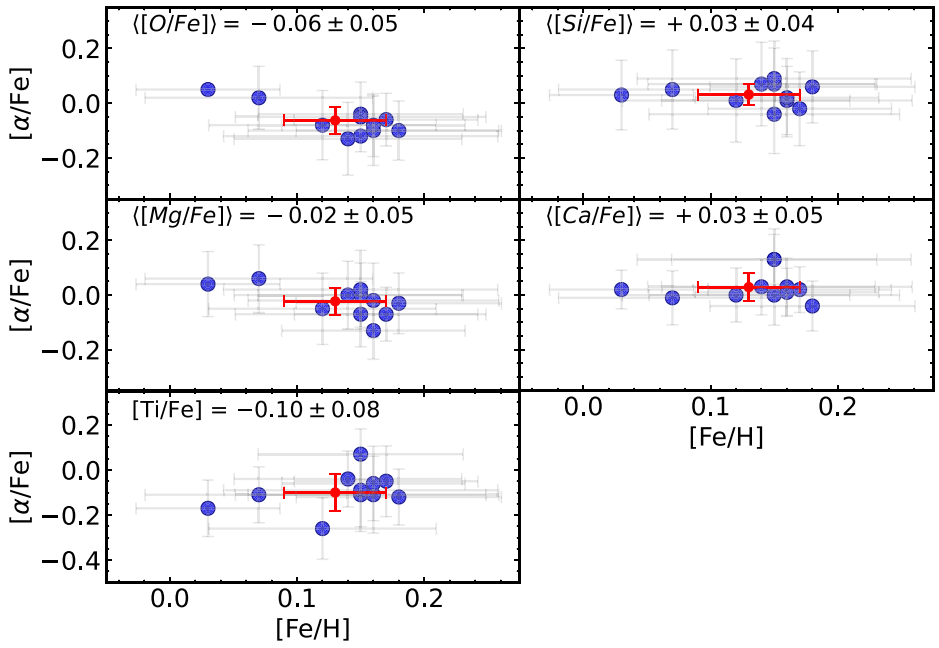

Figure 8. [α/Fe] versus [Fe/H] diagram for NGC 6705 stars. In each panel, the red circle indicates the mean abundance ratios of O, Mg, Si and Ca, and Ti as a function of mean metallicity, with the error bars representing the STD.

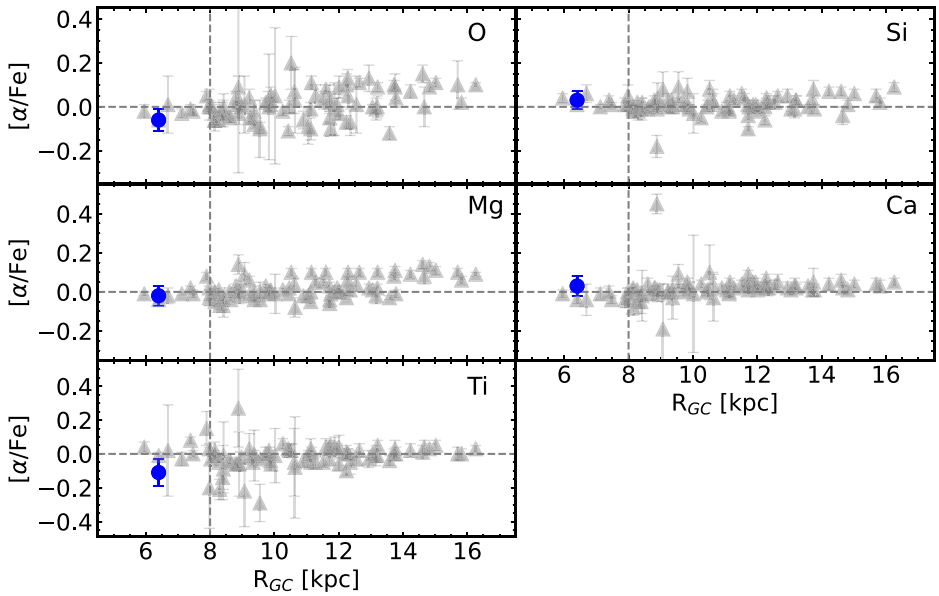

Figure 9. The plot shows the cluster mean abundances of [α/Fe] as a function of the cluster galactocentric distance (x-axis). The grey triangles represent the OCCAM data from Myers et al. 2022, while blue circles represent the results of this work.

from the OCCAM sample (Myers et al. 2022, grey triangles); our results for NGC 6705 are represented by the solid blue circles. The abundances in Myers et al. (2022) are calibrated abundances from DR17, and these were computed using the plane parallel radiative transfer code Synspec and in non-LTE for the elements Mg, Si, and Ca (Osorio et al. 2020). A simple inspection of Fig. 9 shows that the ratios for the five α-elements in NGC 6705 are overall consistent with and do not fall above the results for the other open cluster in the OCCAM sample, and these seem to be in line also with the general trend of metallicity with R_{GC} for the inner galaxy, with all open clusters in the inner galaxy having [α/Fe] ratios roughly around the solar value.

6.3 Na, Al, K, V, Cr, Mn, Co, and Ce abundance patterns

The [X/Fe] versus [Fe/H] ratios for the other studied species besides CNO and α-elements are presented as filled blue circles in Fig. 10, along with abundance results for Galactic field stars from five high-resolution optical studies in the literature (Chen et al. 2000; Adibekyan et al. 2012; Bensby, Feltzing & Oey 2014; Battistini &

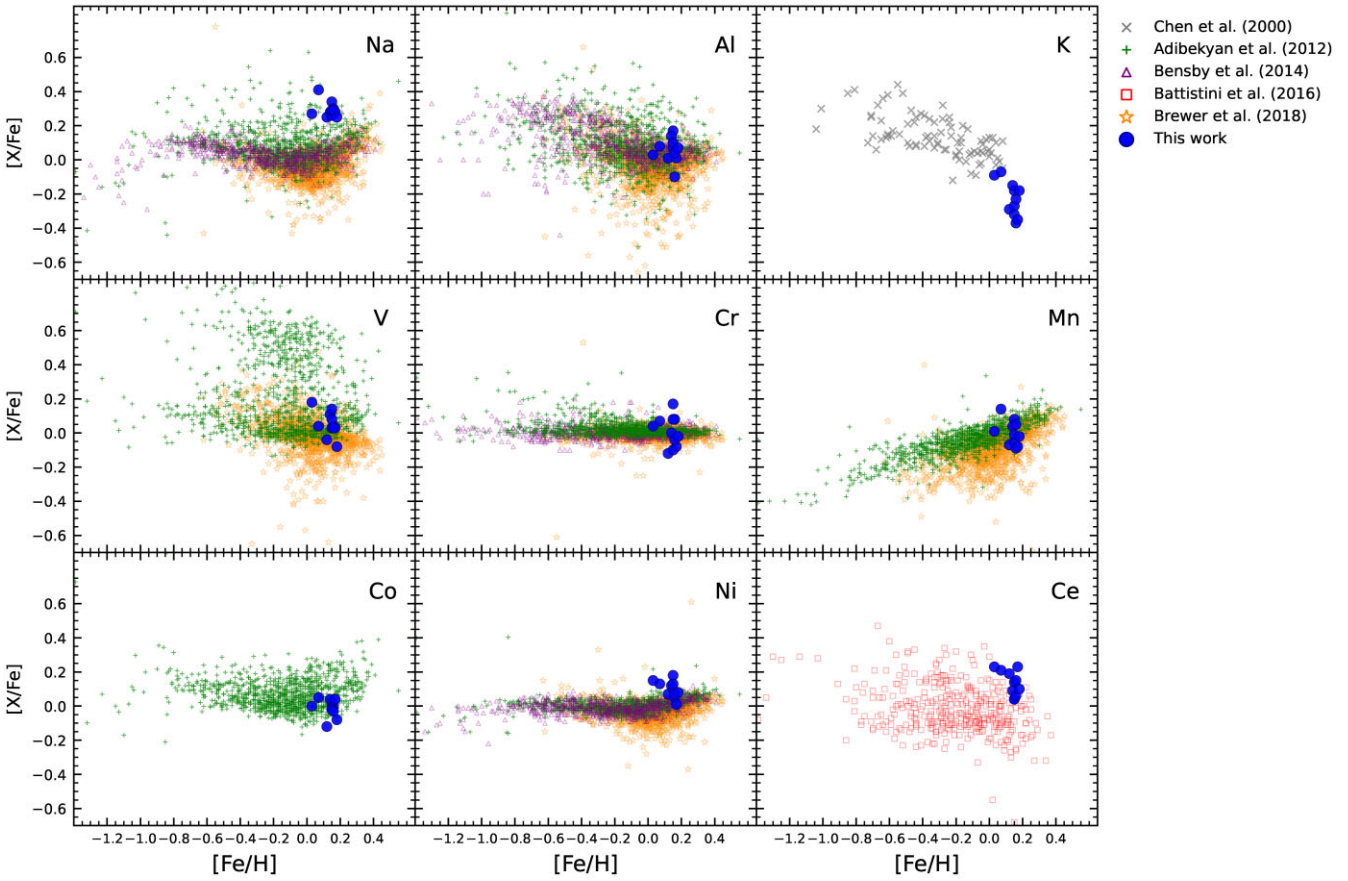

Figure 10. Galactic trends of [X/Fe] as a function of [Fe/H] for the stars in the open cluster NGC 6705 (blue circles). Field dwarf stars in the thin and thick disc are from Chen et al. (2000, grey xs), Adibekyan et al. (2012, green pluses), Bensby et al. (2014, purple triangles), Battistini & Bensby (2016, red squares), and Brewer & Fischer (2018, orange stars).

Bensby 2016; Brewer & Fischer 2018). The three top panels of Fig. 10 show the odd-Z elements Na, Al, and K. The derived Al abundances fall within the field star distribution at [Fe/H] $\sim +0.15$, while for sodium the abundances of NGC 6705 red-giants fall above the trend; this likely is a mixing signature, as discussed in Section 6.1. For K, the metallicity range probed for the field stars (Chen et al. 2000) stops at around solar [Fe/H], and the [K/Fe] values for NGC 6705 simply extend the downward trend of [K/Fe] versus [Fe/H]. For the Fe-peak elements V, Cr, Mn, and Co, our results also generally fall within the field star trends, noting, however, that there is more scatter in our Cr abundances when compared with the very thin (and flat) trend for the field stars obtained from the optical studies. For Ni, the derived abundances for some of the stars fall above the field star trend, the latter being also quite well defined according to the results in Bensby et al. (2014) and Adibekyan et al. (2012).

The only heavy element analysed from APOGEE spectra is the s-process element Ce, which is produced mainly in AGB stars (Cescutti & Matteucci 2022). The [Ce/Fe] versus [Fe/H] abundance pattern for the field stars from Battistini & Bensby (2016), shown as comparisons in Fig. 10, overall exhibits some scatter. The mean Ce abundance obtained for NGC 6705 red giants is enhanced, with $\langle$[Ce/Fe]$\rangle = +0.13 \pm 0.07$, falling in the upper envelope of the abundance distribution of field stars at [Fe/H] > 0.0. In addition, the observed [Ce/Fe] enhancement for NGC 6705 is in-line with previous findings that [Ce/Fe] ratios are a function of age (Casali et al. 2020). The observed chemical pattern resembles the enhancements in [Ce/Fe] observed in other young open clusters, which is larger than typical values of [Ce/Fe] in old open clusters with similar metallicities (see Fig. 6 in Sales-Silva et al. 2022).

7 CONCLUSIONS

NGC 6705 is a young open cluster that serves as an abundance benchmark for the inner Milky Way young stellar populations ($\sim$1–5 $\times$ 10^8 yrs). The red giant members of this cluster are also good stellar samples in which to probe evolution along the RGB and RC in 3–4 $M_\odot$ metal-rich giants.

Previous works in the literature found this benchmark young open cluster to be α-enhanced, a puzzling result as young stars are expected to be formed from material already enriched in Fe from SN Ia, which would result in low values of [α/Fe]. The abundance patterns for NGC 6705 were discussed by Casamiquela et al. (2018) in the context of the population of young and α-enhanced field stars found from CoRoT and Kepler data (Chiappini et al. 2015; Martig et al. 2015; Queiroz et al. 2023).

The population of young-α-enhanced stars identified in the Galaxy, however, has now been shown to be old and to possibly result from binary mergers or mass transfer, as suggested by Izzard et al. (2018) and Hekker & Johnson (2019). This scenario was strengthened by the results of Miglio et al. (2021) from their analysis of old, thick-disc giants in the Kepler field that have been found to be overmassive, meaning that their initial birth masses were increased by mass transfer or mergers while evolving up the RGB.

The possibility that the young cluster NGC 6705 is α-enhanced was further tested here based on the derived abundances of five α-elements (O, Mg, Si, and Ca, and Ti), finding $\langle[\alpha/\mathrm{Fe}]\rangle = -0.025 \pm 0.051$), and indicating that NGC 6705 does not exhibit α-enhancement. Our results are consistent with the expectation that the young open cluster NGC 6705 in the Galactic disc has solar-like values of the [α/Fe] ratio.

This study presented a quantitative spectroscopic analysis of eleven red giant stars members of the open cluster NGC 6705, determining abundances of the elements C, N, Na, Al, K, Ti, V, Cr, Mn, Fe, Co, Ni, and Ce, as well as the α-elements O, Mg, Si, and Ca. The analysis was carried out in LTE, using MARCS spherical model atmospheres with the spherical radiative transfer program Turbospectrum. The mean abundances obtained for the cluster are presented in Table 5.

Our results from the analysis of APOGEE NIR spectra for the NGC 6705 stars find an average metallicity of $\langle[\mathrm{Fe/H}]\rangle = +0.13 \pm 0.04$ dex, which is in agreement with the general trend of increasing metallicity with decreasing distance from the Galactic Centre. The ratios of the Fe-peak elements are found to track Galactic trends, as defined by field stars, with the mean values of [X/Fe] for V, Cr, Mn, Co, and Ni being +0.05, +0.01, 0.00, −0.01, and +0.10, respectively. The [Al/Fe] abundance ratios also fall within the distribution of field stars, while the [K/Fe] values appear to extend the downward trend of [K/Fe] versus [Fe/H]. Results for the s-process element cerium, with $\langle[\mathrm{Ce/Fe}]\rangle = +0.13$, are similar to the Ce abundances observed in other young open clusters with similar metallicities to NGC 6705 and consistent with an increase in the [Ce/Fe] ratio with decreasing age (Sales-Silva et al. 2022).

The red-giant members of NGC 6705 exhibit the low-^{12}C and enhanced-^{14}N abundance signature of 1st dredge-up on the RGB, with mean values of $[^{12}\mathrm{C/Fe}] = -0.16$ and $[^{14}\mathrm{N/Fe}] = +0.51$. These abundances are in quantitative agreement with 3–4.0 $\mathrm{M}_{\odot}$ stellar models from Lagarde et al. (2012). The sample here contains both candidate RGB (7) and RC (4) stars and a comparison of the ^{12}C and ^{14}N abundances between the two groups reveals no significant differences, indicating no measurable 'extra mixing' processes as these metal-rich 3.3 $\mathrm{M}_{\odot}$ stars evolve up the RGB and then onto the He-burning red clump. In addition to carbon-12 and nitrogen-14, oxygen, sodium, and aluminum abundances were compared to stellar models in order to test for deep mixing signatures. Sodium was found to be enhanced significantly with $[\mathrm{Na/Fe}] = +0.29 \pm 0.04$, in general agreement with stellar evolution model predictions from Lagarde et al. (2012) and in-line with what was previously concluded in Smiljanic et al. (2016). For aluminum, however, we find non-enhanced values of [Al/Fe] for NGC 6705, in contrast with what was found in the latter study. The values of [O/Fe] and [Al/Fe] for NGC 6705 were found to be roughly solar, within small uncertainties and a comparison to models by Lagarde et al. (2012) also finds agreement with our O and Al abundance results for stellar masses of 3.3 $\mathrm{M}_{\odot}$. Summarizing, at the masses of the NGC 6705 red giants, standard stellar evolution models agree well with the observationally-derived abundances of ^{12}C, ^{14}N, ^{16}O, Na, and Al.

ACKNOWLEDGEMENTS

We thank the referee for suggestions that improved the paper. VL-T acknowledges the financial support from Coordenação de Aperfeiçoamento de Pessoal de Nível Superior (CAPES). KC acknowledges that her work is supported, in part, by the National Science Foundation through NSF grant No. AST-2206543. DS thanks the National Council for Scientific and Technological Development – CNPq.

Funding for the Sloan Digital Sky Survey IV has been provided by the Alfred P. Sloan Foundation, the U.S. Department of Energy Office of Science, and the Participating Institutions. SDSS-IV acknowledges support and resources from the Center for High-Performance Computing at the University of Utah. The SDSS website is www.sdss.org. SDSS-IV is managed by the Astrophysical Research consortium for the Participating Institutions of the SDSS Collaboration including the Brazilian Participation Group, the Carnegie Institution for Science, Carnegie Mellon University, the Chilean Participation Group, the French Participation Group, Harvard-Smithsonian Center for Astrophysics, Instituto de Astrofísica de Canarias, The Johns Hopkins University, Kavli Institute for the Physics and Mathematics of the Universe (IPMU)/University of Tokyo, Lawrence Berkeley National Laboratory, Leibniz Institut für Astrophysik Potsdam (AIP), Max-Planck-Institut für Astronomie (MPIA Heidelberg), Max-Planck-Institut für Astrophysik (MPA Garching), Max-Planck-Institut für Extraterrestrische Physik (MPE), National Astronomical Observatory of China, New Mexico State University, New York University, University of Notre Dame, Observatório Nacional/MCTI, The Ohio State University, Pennsylvania State University, Shanghai Astronomical Observatory, United Kingdom Participation Group, Universidad Nacional Autónoma de México, University of Arizona, University of Colorado Boulder, University of Oxford, University of Portsmouth, University of Utah, University of Virginia, University of Washington, University of Wisconsin, Vanderbilt University, and Yale University.

Facilities: Sloan, Gaia.

Software: BACCHUS (Masseron et al. 2016), Turbospectrum (Alvarez & Plez 1998; Plez 2012; https://github.com/bertrandplez/Turbospectrum2019).

DATA AVAILABILITY

The data underlying this article are available in the SDSS Data Release 17 for APOGEE (Abdurro'uf et al. 2022). These data can be accessed at the following links: https://www.sdss.org/dr17/irspec/(APOGEE).

REFERENCES

Abdurro'uf et al., 2022, ApJS, 259, 35
Adibekyan V. Z., Sousa S. G., Santos N. C., Delgado Mena E., González Hernández J. I., Israelian G., Mayor M., Khachatryan G., 2012, A&A, 545, A32
Alvarez R., Plez B., 1998, A&A, 330, 1109
Anders F. et al., 2014, A&A, 564, A115
Asplund M., Amarsi A. M., Grevesse N., 2021, A&A, 653, A141
Baglin A., Auvergne M., Barge P., Deleuil M., Catala C., Michel E., Weiss W., Team COROT , 2006, in Fridlund M., Baglin A., Lochard J., Conroy L.eds, The CoRoT Mission Pre-Launch Status—Stellar Seismology and Planet Finding. 1306, ESA Special Publication, p.33
Bailer-Jones C. A. L., Rybizki J., Fouesneau M., Demleitner M., Andrae R., 2021, AJ, 161, 147
Battistini C., Bensby T., 2016, A&A, 586, A49
Beaton R. L. et al., 2021, AJ, 162, 302
Bensby T., Feltzing S., Oey M. S., 2014, A&A, 562, A71
Bertelli Motta C. et al., 2018, MNRAS, 478, 425
Bilir S., Ak S., Karaali S., Cabrera-Lavers A., Chonis T. S., Gaskell C. M., 2008, MNRAS, 384, 1178
Blanton M. R. et al., 2017, AJ, 154, 28
Bressan A., Marigo P., Girardí L., Salasnich B., Dal Cero C., Rubele S., Nanni A., 2012, MNRAS, 427, 127

Brewer J. M., Fischer D. A., 2018, ApJS, 237, 38
Campello R. J. G. B., Moulavi D., Sander J., 2013, in Pei J., Tseng V. S., Cao L., Motoda H., Xu G.eds, Advances in Knowledge Discovery and Data Mining. Springer Berlin Heidelberg, Berlin, Heidelberg, p. 160
Cantat-Gaudin T., Anders F., 2020, A&A, 633, A99
Cantat-Gaudin T. et al., 2014, A&A, 569, A17
Cantat-Gaudin T. et al., 2018, A&A, 618, A93
Cantat-Gaudin T. et al., 2020, A&A, 640, A1
Casali G. et al., 2020, A&A, 639, A127
Casamiquela L. et al., 2016, MNRAS, 458, 3150
Casamiquela L. et al., 2018, A&A, 610, A66
Casamiquela L. et al., 2021, A&A, 652, A25
Cescutti G., Matteucci F., 2022, Universe, 8, 173
Charbonnel C., Lagarde N., 2010, A&A, 522, A10
Chen Y. Q., Nissen P. E., Zhao G., Zhang H. W., Benoni T., 2000, A&AS, 141, 491
Chiappini C. et al., 2015, A&A, 576, L12
Cunha K. et al., 2015, ApJ, 798, L41
Cutri R. M. et al., 2003, 2MASS All Sky Catalog of point sources. available at: http://irsa.ipac.caltech.edu/applications/Gator/
Dias W. S., Monteiro H., Moitinho A., Lépine J. R. D., Carraro G., Paunzen E., Alessi B., Villela L., 2021, MNRAS, 504, 356
Donor J. et al., 2018, AJ, 156, 142
Frinchaboy P. M. et al., 2013, ApJ, 777, L1
Fuhrmann K., 1998, A&A, 338, 161
Gaia Collaboration, 2021, A&A, 649, A1
Gao X. et al., 2018, MNRAS, 481, 2666
García Pérez A. E. et al., 2016, AJ, 151, 144
Gilmore G. et al., 2012, The Messenger, 147, 25
Gilmore G. et al., 2022, A&A, 666, A120
Gonzalez G., Wallerstein G., 2000, PASP, 112, 1081
González Hernández J. I., Bonifacio P., 2009, A&A, 497, 497
Grevesse N., Asplund M., Sauval A. J., 2007, Space Sci. Rev., 130, 105
Gunn J. E. et al., 2006, AJ, 131, 2332
Gustafsson B., Edvardsson B., Eriksson K., Jørgensen U. G., Nordlund Å., Plez B., 2008, A&A, 486, 951
Hayes C. R. et al., 2018, ApJ, 852, 49
Heiter U., Soubiran C., Netopil M., Paunzen E., 2014, A&A, 561, A93
Hekker S., Johnson J. A., 2019, MNRAS, 487, 4343
Hubeny I., Allende Prieto C., Osorio Y., Lanz T., 2021, TLUSTY and SYNSPEC Users's Guide IV: Upgraded Versions 208 and 54. preprint(arXiv:2104.02829)
Hunt E. L., Reffert S., 2023, A&A, 673, A114
Izzard R. G., Preece H., Jofre P., Halabi G. M., Masseron T., Tout C. A., 2018, MNRAS, 473, 2984
Jackson R. J. et al., 2022, MNRAS, 509, 1664
Jofré P. et al., 2023, A&A, 671, A21
Jönsson H. et al., 2020, AJ, 160, 120
Karakas A. I., Lattanzio J. C., 2014, PASA, 31, e030
Lagarde N., Decressin T., Charbonnel C., Eggenberger P., Ekström S., Palacios A., 2012, A&A, 543, A108
Magrini L. et al., 2014, A&A, 563, A44
Magrini L. et al., 2017, A&A, 603, A2
Magrini L. et al., 2021, A&A, 651, A84
Majewski S. R. et al., 2017, AJ, 154, 94
Martig M. et al., 2015, MNRAS, 451, 2230
Masseron T., Merle T., Hawkins K., 2016, BACCHUS: Brussels Automatic Code for Characterizing High accUracy Spectra, Astrophysics Source Code Library, record(ascl:1605.004)
McCormick C. et al., 2023, MNRAS, 524, 4418
Miglio A. et al., 2021, A&A, 645, A85
Montegriffo P., Ferraro F. R., Origlia L., Fusi Pecci F., 1998, MNRAS, 297, 872
Myers N. et al., 2022, AJ, 164, 85
Nidever D. L. et al., 2014, ApJ, 796, 38
Nidever D. L. et al., 2015, AJ, 150, 173
Osorio Y., Allende Prieto C., Hubeny I., Mészáros S., Shetrone M., 2020, A&A, 637, A80

Plez B., 2012, Turbospectrum: Code for spectral synthesis, Astrophysics Source Code Library, record(ascl:1205.004)
Prša A. et al., 2016, AJ, 152, 41
Queiroz A. B. A. et al., 2020, A&A, 638, A76
Queiroz A. B. A. et al., 2023, A&A, 673, A155
Randich S. et al., 2022, A&A, 666, A121
Reddy B. E., Lambert D. L., Allende Prieto C., 2006, MNRAS, 367, 1329
Sales-Silva J. V. et al., 2022, ApJ, 926, 154
Silva Aguirre V. et al., 2018, MNRAS, 475, 5487
Smiljanic R. et al., 2016, A&A, 589, A115
Smith V. V. et al., 2013, ApJ, 765, 16
Smith V. V. et al., 2021, AJ, 161, 254
Souto D. et al., 2016, ApJ, 830, 35
Souto D. et al., 2018, ApJ, 857, 14
Tarricq Y. et al., 2021, A&A, 647, A19
Tautvaišienė G. et al., 2015, A&A, 573. A55
Wannier P. G., Andersson B. G., Olofsson H., Ukita N., Young K., 1991, ApJ, 380, 593
Wilson J. C. et al., 2010, SPIE, 7735, 77351C
Wilson J. C. et al., 2019, PASP, 131, 055001
Zacharias N., Monet D. G., Levine S. E., Urban S. E., Gaume R., Wycoff G. L., 2004, American Astronomical Society Meeting Abstracts, 205, 48
Zasowski G. et al., 2013, AJ, 146, 81
Zasowski G. et al., 2017, AJ, 154, 198

[1]*Observatório Nacional, Rua General José Cristino, 77, 20921-400 São Cristóvão, Rio de Janeiro, RJ, Brazil*
[2]*Steward Observatory, University of Arizona, 933 North Cherry Avenue, Tucson, AZ 85721-0065, USA*
[3]*Institut d'Astrophysique de Paris, UMR7095 CNRS, Sorbonne Université, 98bis Bd. Arago, F-75014 Paris, France*
[4]*Departamento de Física, Universidade Federal de Sergipe, Av. Marechal Rondon, S/N, 49000-000 São Cristóvão, SE, Brazil*
[5]*NSF's NOIRLab, 950 N. Cherry Ave. Tucson, AZ 85719, USA*
[6]*Leibniz-Institut für Astrophysik Potsdam (AIP), An der Sternwarte 16, D-14482 Potsdam, Germany*
[7]*Center for Computational Astrophysics, Flatiron Institute,162 Fifth Avenue, New York, NY 10010, USA*
[8]*Departamento de Astrofísica, Universidad de La Laguna, E-38206 La Laguna, Tenerife, Spain*
[9]*The Observatories of the Carnegie Institution for Science, 813 Santa Barbara Street, Pasadena, CA 91101, USA*
[10]*Apache Point Observatory and New Mexico State University, P.O. Box 59, Sunspot, NM 88349-0059, USA*
[11]*Sternberg Astronomical Institute, Moscow State University, 119234, Moscow, Russia*
[12]*Department of Physics & Astronomy, Texas Christian University, TCU Box 298840, Fort Worth, TX 76129, USA*
[13]*Space Telescope Science Institute, 3700 San Martin Drive, Baltimore, MD 21218, USA*
[14]*NRC Herzberg Astronomy and Astrophysics Research Centre, 5071 West Saanich Road, Victoria, B.C., Canada, V9E 2E7*
[15]*New Mexico State University, Las Cruces, NM 88003, USA*
[16]*Materials Science and Applied Mathematics, Malmö University, SE-205 06 Malmö, Sweden*
[17]*Department of Astronomy, University of Virginia, Charlottesville, VA 22904-4325, USA*
[18]*ELTE Eötvös Loránd University, Gothard Astrophysical Observatory, 9700 Szombathely, Szent Imre H. st. 112, Hungary*
[19]*MTA-ELTE Lendület 'Momentum' Milky Way Research Group, Hungary*
[20]*Department of Physics, Montana State University, P.O. Box 173840, Bozeman, MT 59717-3840*
[21]*Department of Astronomy, The Ohio State University, Columbus, OH 43210, USA*
[22]*Department of Physics and Astronomy, University of Utah, Salt Lake City, UT 84105, USA*

This paper has been typeset from a TEX/LATEX file prepared by the author.